THERMAL STABILITY AND DEFECT STRUCTURE OF HOT-WIRE DEPOSITED AMORPHOUS SILICON

by

CHRISTOPHER JOSEPH ARENDSE

Submitted in partial fulfilment of
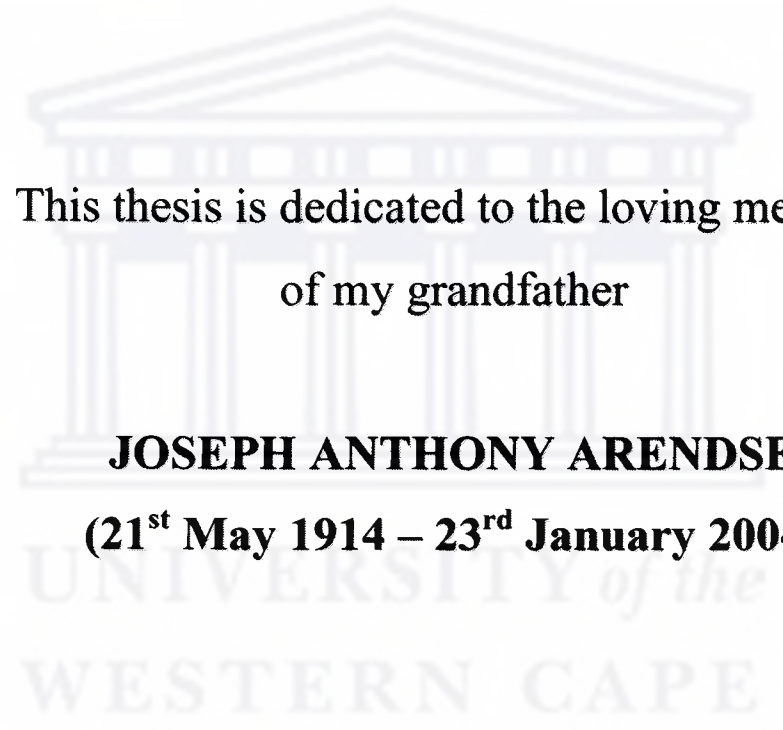the requirements of the degree of

PHILOSOPHIAE DOCTOR

in the

DEPARTMENT OF PHYSICS
UNIVERSITY OF THE WESTERN CAPE

SUPERVISOR : PROF. D. KNOESEN

JANUARY 2004

i

This thesis is dedicated to the loving memory

of my grandfather

JOSEPH ANTHONY ARENDSE

(21st May 1914 – 23rd January 2004)

KEY WORDS

**THERMAL STABILITY AND DEFECT STRUCTURE OF
HOT-WIRE DEPOSITED AMORPHOUS SILICON**

CHRISTOPHER JOSEPH ARENDSE

Amorphous silicon

Hot-wire chemical vapour deposition

Staebler-Wronski Effect

Hydrogen diffusion

Microstructure

Microvoids

Raman scattering

Structural order

Phase transition

Doppler-broadening spectroscopy

ABSTRACT

THERMAL STABILITY AND DEFECT STRUCTURE OF HOT-WIRE DEPOSITED AMORPHOUS SILICON

CHRISTOPHER JOSEPH ARENDSE

Ph.D. Thesis, Department of Physics, University of the Western Cape

Hydrogenated amorphous silicon (a-Si:H) thin films are presently used in several large-area thin-film applications. However, one major concern of a-Si:H is the fact that the stability of the material degrades when it is exposed to prolonged sunlight illumination. This effect, referred to as the Staebler-Wronski effect (SWE), is however reduced when using hot-wire (HW) deposited a-Si:H material with a low hydrogen concentration and favourable microstructure. In this thesis we report on the thermal stability of HW-deposited a-Si:H thin films, with different H-concentrations and bonding configurations, when exposed to elevated temperatures in excess of 100 °C.

In this study we propose a model that describes how the thermal stability is influenced by the migration and bonding behaviour of hydrogen. Infrared spectroscopy and Raman scattering analyses provide evidence that the original site of hydrogen emission is the $\equiv$Si–H bond, caused primarily by an increase in the network disorder, which consequently results in a reduction of the $\equiv$Si–H bond strength and the optical band gap. Furthermore, this mechanism results in the creation of hydrogen-terminated silicon dangling bonds that eventually align to form low concentrations of larger open-volume defects or microvoids, as probed by Doppler-broadening and positron lifetime spectroscopy.

JANUARY 2004

DECLARATION

I declare that

"THERMAL STABILITY AND DEFECT STRUCTURE OF HOT-WIRE DEPOSITED AMORPHOUS SILICON"

is my own work, that it has not been submitted for any degree or examination in any other university, and that all the sources I have used or quoted have been indicated and acknowledged by means of complete references.

CHRISTOPHER JOSEPH ARENDSE   **JANUARY 2004**

SIGNED: ....

v
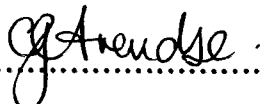
ACKNOWLEDGEMENTS

I am very grateful to the following people and organisations without whose assistance, advice and guidance this thesis would not have been possible.

Prof. Dirk Knoesen (Department of Physics, University of the Western Cape) for the excellent supervision of this thesis, his guidance, encouragement, friendship and for the many stimulating discussions.

Prof. Werner van der Weg (Department of Interface Physics, Utrecht University), who acted as supervisor during my stay in Utrecht and as co-supervisor, for his guidance, friendship and many fruitful discussions.

Prof. Ruud Schropp and Dr. Anke Brockhoff (Department of Interface Physics, Utrecht University) for their unselfish help with the Raman scattering experiments and analysis and for the many fruitful discussions around this investigation.

Prof. Ryno Swanepoel (Department of Physics, University of the Western Cape) for his interest in this investigation, for his assistance with the depositions and the analyses of the optical transmission data.

Prof. David Britton, Dr. Mike Osiele and Miss. Anne Dabrowski (Department of Physics, University of Cape Town) for the positron annihilation measurements and analysis.

Dr. Chris Theron and Mr. Karl Springhorn (Materials Research Group, *i*Themba Labs) for their assistance with the ERD measurements and analysis.

Thank you!

CONTENTS

CHAPTER 1

Introduction

1.1 HYDROGENATED AMORPHOUS SILICON

Silicon is bonded covalently in both its crystalline and amorphous phases. The structure of amorphous silicon is believed to be a random network with four-coordinated atoms in their local bonding configuration [1.1]. Amorphous silicon (a-Si), in contrast to crystalline silicon (c-Si), is not homogeneous in the long-range order due to defects and vacancies present in the amorphous network [1.2]. This results in a-Si behaving like a direct band gap semiconductor and consequently having a much higher absorption coefficient, about 10^4 cm^{-1} at an energy of 2 eV, compared to that of c-Si.

A schematic representation of the density of states (DOS) in a-Si is shown in Figure 1.1. The average Si–Si bond angle and inter-atomic distance in a-Si deviate from the ideal tetrahedral structure, which causes a broadening of the valence and conduction bands into the band gap and consequently resulting in tail states at the band edges. The average bond angle in a-Si deviate by 7° – 14° from the tetrahedral value of 109.5° [1.3]. The average bond length in a-Si is about 1.9 %

longer than that in c-Si, resulting in a volume expansion and consequently in a reduction in the mass density, of about 1.8 % less dense than c-Si [1.4].

A prominent feature in the DOS of a-Si is the presence of defect states in the mid band gap. This is primarily due to the three-fold coordinated silicon atoms, which results in the presence of dangling bonds. These dangling bonds can act as efficient traps, thereby diminishing the electronic properties of the material. In pure a-Si the dangling bond density is of the order of 10^{20} cm^{-3} [1.5] and this can be reduced by introducing hydrogen into the a-Si network. The essential role of hydrogen in a-Si is its ability to passivate the dangling bonds. The resulting material is referred to as hydrogenated amorphous silicon (a-Si:H). Hydrogenation to a level of about 10 at.% reduces the defect density by several orders of magnitude to about 5×10^{15} cm^{-3}. Hydrogenation not only reduces the defect density in a-Si, but also provides more structural relaxation, as seen by the reduction in the disorder present in a-Si:H [1.1]. Figure 1.2 draws a comparison between the structure of c-Si and a-Si:H.
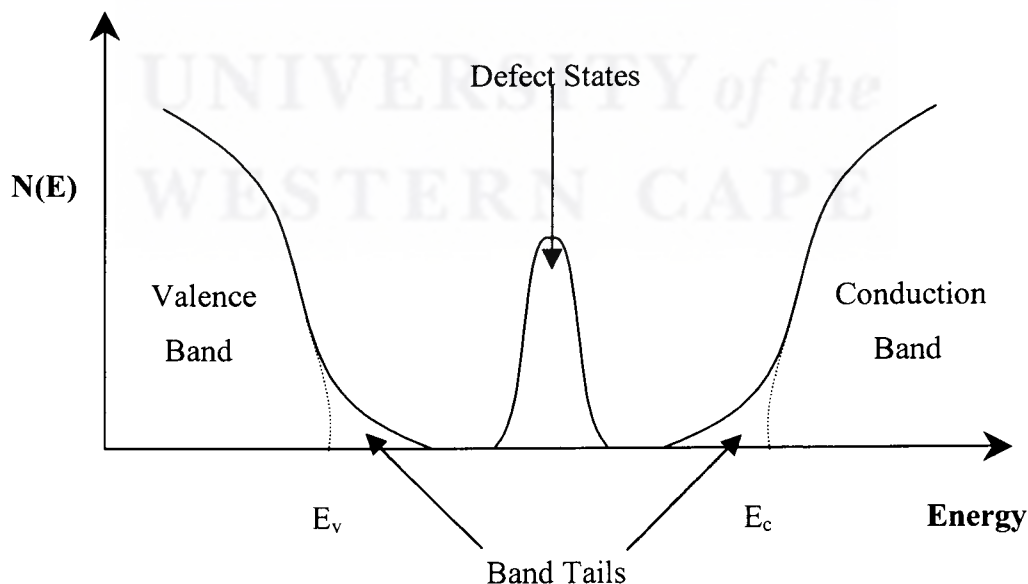
Figure 1.1   Schematic representation of the density of states in amorphous silicon.

The opto-electronic properties of a-Si:H critically depends on the preparation technique, deposition conditions and thermal history. Acco *et al.* [1.6 – 1.7] have shown that the solubility for hydrogen in a-Si:H prepared by ion implantation is about 4 at.%. When this solubility level is exceeded, the amorphous structure becomes unstable to inhomogeneity formation and, upon annealing at 400 °C, nanoscale H-rich defects or nanovoids nucleate and grow in size [1.7 – 1.8].
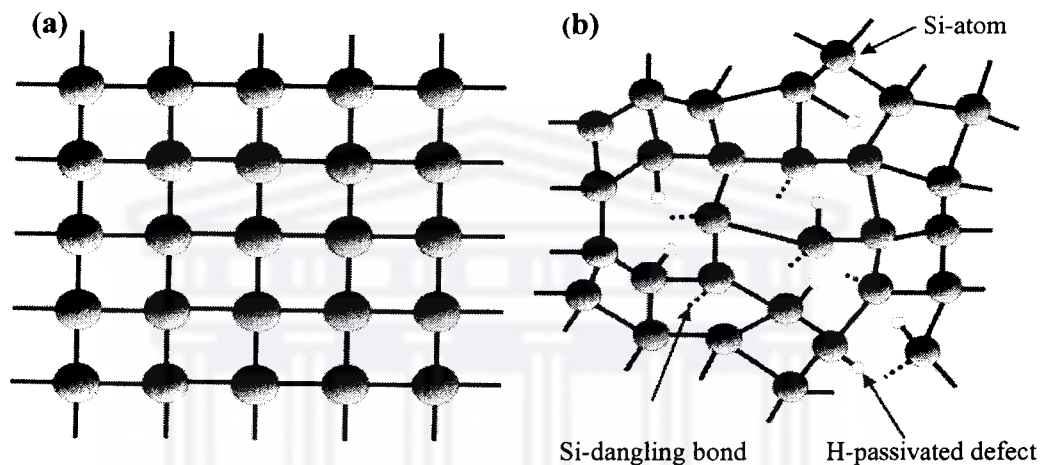
Figure 1.2   Comparison between the structure of (a) c-Si and (b) a-Si:H.

Device-quality a-Si:H deposited by glow discharge (GD) and hot-wire (HW) chemical vapour deposition contains about 10 at.% and 2 at.% hydrogen respectively [1.1, 1.9]. Small-angle x-ray scattering (SAXS) measurements supplemented by flotation analysis revealed that a-Si:H is not homogeneous, but contains low density nanovoids with typical sizes of 1 – 10 nm embedded in the amorphous network [1.10]. However, it has been shown that the nanovoid concentration for GD and HW a-Si:H grown at deposition temperatures of 250 °C and 390 °C respectively are below the present SAXS detection limit of 0.01 vol.% [1.8, 1.11]. At growth temperatures below 300 °C, HW a-Si:H contains a significant fraction of larger microvoids as compared to that of GD a-Si:H grown at the same temperature [1.9].

A crucial prerequisite for the understanding of the microstructure in a-Si:H is an understanding of the hydrogen distribution in the amorphous network. Nuclear magnetic resonance (NMR) measurements provided evidence that the spatial distribution of hydrogen in a-Si:H is not homogeneous, where two separate hydrogen phases have been identified [1.12 – 1.14]. The first is the isolated phase, corresponding to $\equiv$Si–H monohydrides that are well separated from each other. The second phase contains the remainder of the hydrogen and consists of small volumes of clustered hydrogen, which are present in $\equiv$Si–H bonds on void surfaces, $=$Si$=$H$_2$ dihydrides and $(=$Si$=$H$_2)_n$ polyhydrides. Device-quality GD a-Si:H typically contains 5 – 7 hydrogen atoms per cluster and these clusters are well separated from each other. Contrary to this, Wu *et al.* [1.15] have shown that the microstructure of clustered hydrogen in device-quality HW a-Si:H, with an H-concentration of less than 4 at.%, is quite different. The large hydrogen clusters in this material contains at least 14 hydrogen atoms per cluster, which accounts for about 90 % of the total bonded hydrogen concentration. The different microstructure of device-quality HW a-Si:H deposited at high growth temperatures is due to an improved structural order, and consequently a lower fraction of hydrogen is required for structural relaxation [1.15], which is below the solubility level in a-Si:H prepared by ion implantation.

With the first deposition of a-Si:H in 1965 [1.16] it was assumed that any donor and acceptor atoms would not be active in the material, since it was believed that the dopant atoms would always find a lattice site where they are electrically inactive. However, in 1975 Spear and LeComber showed that it was possible to dope GD a-Si:H by introducing diborane (for p-type material) and phosphine (for n-type material) to the deposition chamber [1.17]. It was found that the doping efficiency, which is defined as the fraction of the introduced dopant atoms that are electrically active, is extremely low for a-Si:H. For c-Si the doping efficiency is of the order of unity, whereas in a-Si:H it can range from 10^{-4} to 10^{-2}, depending on the deposition conditions. Thus, for a-Si:H more dopant atoms have to be incorporated into the reaction chamber as compared to c-Si. This breakthrough made a-Si:H suitable for various technological applications and resulted in a rapid

increase of research activities in this field. Shortly after this discovery the first a-Si:H solar cell was produced, which consisted of an intrinsic layer sandwiched between a p-type and n-type doped layer [1.18].

1.2 METASTABILITY: THE STAEBLER-WRONSKY EFFECT

One major drawback of a-Si:H, and subsequently devices made from this material, is the fact that the electronic properties of the material degrade when it is exposed to prolonged sunlight illumination. The first observation of the degradation dates back to 1977, where Staebler and Wronski observed that the dark-conductivity and photo-conductivity of GD a-Si:H are significantly reduced under prolonged illumination by an intense light source [1.19]. This light-induced effect is known as the so-called Staebler-Wronski Effect (SWE), which manifests itself by an increase in the dangling bond density from less than 10^{16} cm^{-3} in intrinsic a-Si:H to about 10^{17} cm^{-3} [1.1, 1.20]. However, the SWE is a self-limiting process; i.e. the defect density saturates after a long time. These defects are metastable and can be reversed by annealing at moderate temperatures in excess of 150 °C for several hours.

The dangling bond density, N_{db}, under prolonged illumination is related to the light-soaking time, t, by [1.21]:

$$N_{db}(t) \propto G^{2/3} t^{1/3} \qquad (1.1)$$

where G refers to the generation rate of the dangling bonds.

It has been shown that the SWE is critically dependent on the H-concentration and hydrogen distribution in a-Si:H. Films with low H-concentrations and favourable microstructure show a reduced degradation. Regardless of the many mechanisms

that have been put forward to explain the light-induced metastability of a-Si:H, an unambiguous microscopic model for the SWE has not yet been identified [1.22 – 1.27].

Kamei *et al.* [1.28] have successfully demonstrated that the SWE is not caused by impurities in the material, since the effect was also observed in pure a-Si. This is a direct proof that the SWE is intrinsic to a-Si:H and it does not depend on the concentration of the major impurities below a critical value of about 10^{19} cm^{-3}. It has been established that the SWE is a bulk effect and that the driving force behind it is the non-radiative recombination of photo-generated charge carriers at metastable defect sites [1.29], identified later as the $\equiv$Si–H bond [1.25].

The most recent and promising model for the SWE has been proposed by Branz [1.25 – 1.26], providing a direct link between hydrogen diffusion and metastable defect creation. If an electron-hole pair recombines in the vicinity of an $\equiv$Si–H bond, the recombination energy is used to excite the hydrogen atom into a mobile state, since the recombination energy is of the same order as the activation energy for hydrogen diffusion. The mobile hydrogen then diffuses interstitially through the amorphous network, leaving behind a Si dangling bond that is indistinguishable from native dangling bonds. Each reactive mobile hydrogen atom breaks a strained Si–Si bond and consequently results in the formation of a weak $\equiv$Si–H bond and two Si dangling bonds. A schematic of this model for the SWE is illustrated in Figure 1.3. When two mobile hydrogen atoms collide, an immobile metastable two-hydrogen complex is formed and eventually becomes trapped in H-rich clusters or voids [1.6 – 1.8].

In conclusion, even though there is no universal consensus about the microscopic origin for the SWE, it is generally believed that the main cause is the recombination processes that result in the creation of metastable Si dangling bonds.
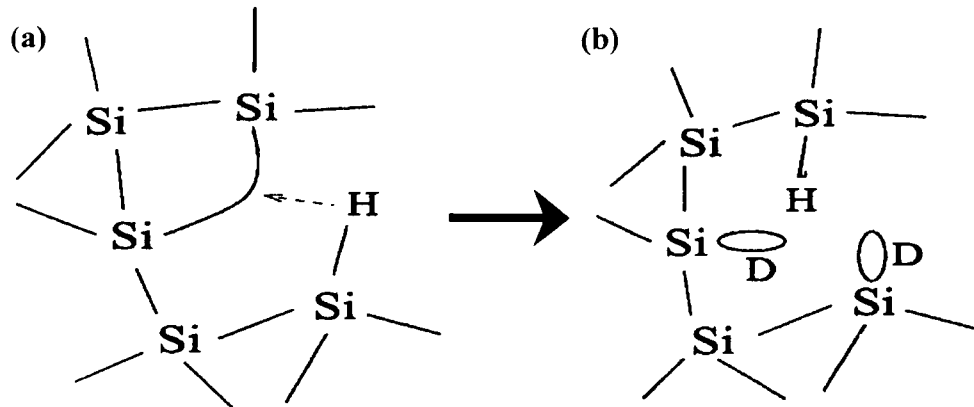
Figure 1.3   A schematic illustration of the SWE, showing (a) the breaking of the ≡Si–H bond and diffusion of hydrogen; and (b) the creation of two Si dangling bonds (D) after mobile hydrogen breaks a strained Si–Si bond and consequently forming a weak ≡Si–H bond [1.30].

1.3 DEPOSITION

Until recently, plasma enhanced chemical vapour deposition (PECVD) was the most commonly used technique for the deposition of a-Si:H. In this technique silane gas (SiH_4) dissociates in a radio-frequent (RF) electric field, with a typical frequency of 13.56 MHz, applied in vacuum between two electrodes. The Si–H_x (x =1,2,3) radicals present in the plasma are collected on a substrate, e.g. glass, which is attached to the grounded upper electrode. The temperature of the substrate, typically between 100 – 300 °C, is one of the most important parameters which determines the eventual structure and quality of the deposited a-Si:H film.

A new technique for the deposition of a-Si:H was introduced by Wiesmann *et al.* in 1979 [1.31]. This technique relies on the catalytic decomposition of SiH_4 into Si–H_x (x =1,2,3) radicals by a hot-wire filament. The filaments are made of tungsten (W) or tantalum (Ta), usually at temperatures between 1600 – 2000 °C.

This technique is referred to as the hot-wire chemical vapour deposition (HWCVD) process or catalytic chemical vapour deposition (Cat-CVD). Details of the mechanisms influencing the hot-wire deposition of a-Si:H are discussed elsewhere [1.32 – 1.33]. The HWCVD process is complicated, due to the many variables in the deposition process which must be controlled to deposit device-quality a-Si:H; e.g. deposition pressure, substrate temperature, gas flow rate, gas mixture and the geometry of the deposition chamber.

The a-Si:H films deposited by Wiesmann *et al.* [1.31] were of poor-quality, primarily due to deposition at high pressures. Later, Matsumura [1.34] showed that device-quality a-Si:H films can be deposited at a substrate temperature of 300°C with a deposition rate of about 5 Å/s. In 1989 he showed that the H-concentration of device-quality HW a-Si:H is as low as 3 at.% [1.35]. Following this work, Mahan *et al.* [1.36] deposited device-quality HW a-Si:H with opto-electronic properties equal to or better than that of conventional GD a-Si:H, particularly with H-concentrations as low as 1 at.%. Intrinsic HW a-Si:H layers have been successfully incorporated into solar cell technology [1.37 – 1.38] and show a reduced degradation upon light soaking as compared to devices with GD intrinsic layers [1.39 – 1.40]. This reduced SWE is attributed to the low H-concentration in HW a-Si:H as compared to that of conventional GD a-Si:H. The efficiency of solar cells with HW intrinsic a-Si:H layers typically ranges between 5 – 10 %.

The fact that device-quality a-Si:H films with low H-concentrations can be deposited at high deposition rates by the HWCVD process, makes this technique worth studying from an applications point of view, especially for solar cell production.

1.4 AIMS AND OUTLINE

Today, a-Si:H is successfully used in several large-area thin-film applications, like liquid crystal displays, photocopiers and solar cells. However, as mentioned before, one major concern of a-Si:H, and subsequently devices made from this material, is the fact that that the stability of the material degrades when it is exposed to prolonged illumination. In the manufacturing of the devices the intrinsic a-Si:H layer is usually subjected to further heat treatments, e.g. post-deposition of the n- and p-layers. Furthermore, in subsequent use the devices may also be exposed to radiation and temperature cycling over a wide range of temperatures. Due to the above-mentioned complications, it is of cardinal importance to investigate the stability of hot-wire deposited a-Si:H, not only when exposed to prolonged illumination, but also when exposed to elevated temperatures.

In this thesis, we report on a comparative study of the thermal stability of a-Si:H with different H-concentrations and bonding configurations. The primary aim of our work is to investigate the influence of the as-deposited H-concentration and bonding configuration on the changes in the microstructure, structural disorder, optical band gap and defect structure when exposed to temperatures in excess of 100 °C.

The two extreme materials we have used are device-quality a-Si:H, with low H-concentration and superior microstructure, and poor-quality a-Si:H, with high H-concentration and inferior microstructure, both deposited by the HWCVD process. In general there is no technological application for poor-quality material, but from a scientific point of view is it important since many phenomena that are observed in device-quality material are dramatically enhanced in poor-quality material.

The structure of this thesis is as follows:

Chapter 2 deals with the basics of the MVSYSTEMS HWCVD reaction chamber and the various analytical techniques used to characterise the a-Si:H films. Understanding these techniques is important for the interpretation of the results of the various experiments. Particular emphasis will be placed on positron annihilation and Raman scattering, since these techniques are not widely used in the research of a-Si:H.

In *Chapter 3* we report on the effects of isochronal annealing on the infrared absorption spectra of the a-Si:H films. We will focus on the influence of the initial H-concentration on changes in the hydrogen bonding configuration and migration. *Chapter 4* focuses mainly on the effects of isochronal annealing on the phase transitions and, more importantly, on the structural disorder present in the films, using Raman scattering. We will relate the structural disorder to the changes in H-concentration, and moreover, investigate the effect of H-concentration and structural disorder on the optical band gap.

In *Chapter 5* we report on the effects of isochronal annealing on changes in the defect structure, using Doppler-broadening positron annihilation spectroscopy. This technique is able to detect the changes in the size and concentration of the defects present in the material and, moreover, provide information on types of defects present in the material. The changes in the defect structure will be related to the H-concentration and structural disorder present in films. Finally, we will provide a possible microscopic model for the thermal stability of hot-wire deposited a-Si:H.

General concluding remarks will follow in the *Summary*.

REFERENCES

[1.1]   R. A. Street, in "Hydrogenated Amorphous Silicon", Cambridge University Press, Cambridge UK (1991)

[1.2]   G. N. van den Hoven, Z. N. Liang, L. Nielsen and J. S. Custer, Phys. Rev. Lett. **68** (1992) 3714

[1.3]   A. J. M. Berntsen, in "Structural Disorder in Pure and Hydrogenated Amorphous Silicon", Ph.D. thesis, Utrecht University, Utrecht, The Netherlands (1993)

[1.4]   D. L. Williamson, S. Roorda, M. Chicoine, T. Tabti, P. A. Stolk, S. Acco and F. W. Saris, Appl. Phys. Lett. **67** (1995) 226

[1.5]   R. A. Street, J. C. Knights and D. Biegelsen, Phys. Rev. **B 18** (1978) 1880

[1.6]   S. Acco, D. L. Williamson, P. A. Stolk, F. W. Saris, M. J. van den Boogaard, W. C. Sinke, W. F. van der Weg, S Roorda and P. C. Zalm, Phys Rev. **B 53** (1996) 4415

[1.7]   S. Acco, in "Structural Defects and Hydrogen Clustering in Amorphous Silicon", Ph.D. thesis, Utrecht University, Utrecht, The Netherlands (1997)

[1.8]   S. Acco, W. G. Sark, W. F. van der Weg, D. L. Williamson, S. Roorda and A. Polman, J. Non-Cryst. Solids **227 – 230** (1998) 128

[1.9]   M. Vaněček, A. H. Mahan, B. P. Nelson and R. S. Crandall, Proceedings of the 11th E. C. Photovoltaic Solar Energy Conference, edited by L. Guimaraes, Harwood, Switzerland (1993) 96

[1.10] A. H. Mahan, D. L. Williamson, B. P. Nelson and R. S. Crandall, Phys. Rev. **B 40** (1989) 12024

[1.11] D. L. Williamson, in "Amorphous Silicon Technology – 1995", edited by M. Hack, E. A. Shiffa, M. Powell, A. Matsuda and A. Madan, Materials Research Society, Pittsburgh (1995) 251

[1.12] J. A. Reimer, R. W. Vaughan and J. C. Knights, Phys. Rev. Lett. **44** (1980) 193

[1.13]   J. A. Reimer, R. W. Vaughan and J. C. Knights, Phys. Rev. **B 23** (1981) 2567

[1.14]   J. A. Reimer, R. W. Vaughan and J. C. Knights, Phys. Rev. **B 24** (1981) 3360

[1.15]   Y. Wu, J. T. Stephen, D. X. Han, J. M. Rutland, R. S. Crandall and A. H. Mahan, Phys. Rev. Lett. **77** (1996) 2049

[1.16]   H. F. Sterling and R. C. G. Swann, Solid State Electronics **8** (1965) 653

[1.17]   W. E. Spear and P. G. LeComber, Solid State Comm. **17** (1975) 1193

[1.18]   D. E. Carlson and C. R. Wronski, Appl. Phys. Lett. **28** (1976) 671

[1.19]   D. L. Staebler and C. R. Wronski, Appl. Phys. Lett. **31** (1977) 292

[1.20]   H. Dersch, J. Stuke and J. Beichler, Appl. Phys. Lett. **38** (1980) 456

[1.21]   M. Stutzmann, W. B. Jackson and C. C. Tsai, Appl. Phys. Lett. **45** (1984) 1075

[1.22]   R. Biswas and B. C. Pan, Appl. Phys. Lett. **72** (1998) 371

[1.23]   R. Biswas, Qiming Li, B. C. Pan and Y Yoon, Phys. Rev. **B 57** (1998) 2253

[1.24]   C. Godet, Philos. Mag. **B 77** (1998) 765

[1.25]   M. H. Branz, Solid State Comm. **105** (1998) 387

[1.26]   M. H. Branz, Phys. Rev. **B 59** (1999) 5498

[1.27]   X. Zou, Y. C. Chan, D. P. Webb, Y. W. Lam, Y. F. Hu, C. D. Beling, S. Fung and H. M. Weng, Phys. Rev Lett. **84** (2000) 769

[1.28]   T. Kamei, N. Hata, A. Matsuda, T. Uchiyama, S. Amano, K. Tsukamoto, Y. Yoshioka and T. Hirao, Appl. Phys. Lett. **68** (1996) 2380

[1.29]   M. Stutzmann, W. B. Jackson and C. C. Tsai, Phys. Rev. **B 32** (1985) 23

[1.30]   Z. Remeš, in "Study of Defects and Microstructure of Amorphous and Microcrystalline Silicon Thin Films and Polycrystalline Diamond using Optical Methods", Ph.D. thesis, Charles University, Prague, Czech Republic (1999)

[1.31]   H. Wiesmann, A. K. Ghosh, T. McMahon and M. Strongin, J. Appl. Phys. **50** (1979) 3752

[1.32]   E. C. Molenbroek, A. H. Mahan and A. Gallagher, J. Appl. Phys. **82** (1997) 1909

[1.33]   K. F. Feenstra, in "Hot-wire Chemical Vapour Deposition of Amorphous Silicon and the Applications in Solar Cells", Ph.D. thesis, Utrecht University, Utrecht, The Netherlands (1998)

[1.34]   H. Matsumura, Jpn. J. Appl. Phys. **25(12)** (1986) L949

[1.35]   H. Matsumura, J. Appl. Phys. **65** (1989) 4396

[1.36]   A. H. Mahan, J. Carapella, B. P. Nelson, R. S. Crandall and I. Balberg, J. Appl. Phys. **69** (1991) 6728

[1.37]   B. P. Nelson, E. Iwaniczko, R. E. I. Schropp, A. H. Mahan, E. C. Molenbroek, S. Salamon and R. S. Crandall, Proceedings of the 12th E. C. Photovoltaic Solar Energy Conference Vol. I, edited by R. Hill, W. Palz and P. Helm, H. S. Stephens and Associates, UK (1994) 679

[1.38]   R. E. I. Schropp, K. F. Feenstra, E. C. Molenbroek, H. Meiling and J. K. Rath, Phil. Mag. **B 76** (1997) 309

[1.39]   A. H. Mahan, J. Carapella, B. P. Nelson, R. S. Crandall and I. Balgerg, J. Appl. Phys. **69** (1991) 6728

[1.40]   P. Papadopoulos, A. Scholz, S. Bauer, B. Schröder and H. Öchsner, J. Non-Cryst. Solids **164 – 166** (1993) 87

CHAPTER 2

Experimental Techniques

2.1 INTRODUCTION

This chapter provides a description of the hot-wire reactor chamber used for the deposition of the a-Si:H samples and of the analytical techniques used to characterise the samples under investigation in this thesis. Techniques widely known and long applied to the research of amorphous silicon will be briefly discussed. Particular emphasis will be placed on positron annihilation, Raman scattering and elastic recoil detection. The relevance of these techniques to this study will be discussed in a brief introduction, followed by a theoretical background and the experimental set-up. The data analysis procedures of each technique will be discussed later in the relevant chapters.

2.2 THIN FILM DEPOSITION

2.2.1 THE MVSYSTEMS HOT-WIRE REACTION CHAMBER

The MVSYSTEMS hot-wire CVD system [2.1 – 2.2] is specifically designed for the production of high quality thin film semiconductors and devices. The deposition process occurs primarily in an ultrahigh vacuum (UHV) reaction chamber, capable of achieving a pressure of 10^{-7} Pa. The reaction chamber is made of a welded 304

stainless steel construction complete with CF flanges with copper gaskets to connect the pumps, heater well, gate valve, gas supply and exhaust, view ports and instrumentation. A cross-sectional view of the reaction chamber is given in Figure 2.1. The system has a 1250 W substrate heater, mounted in a well on the top flange of the chamber. A panel-mounted controller with a type K thermocouple attached to the bottom of the heater well controls the temperature of the substrate heater. A stainless steel backing plate, placed against the back of the substrate holder, is used to ensure a homogeneous substrate temperature.
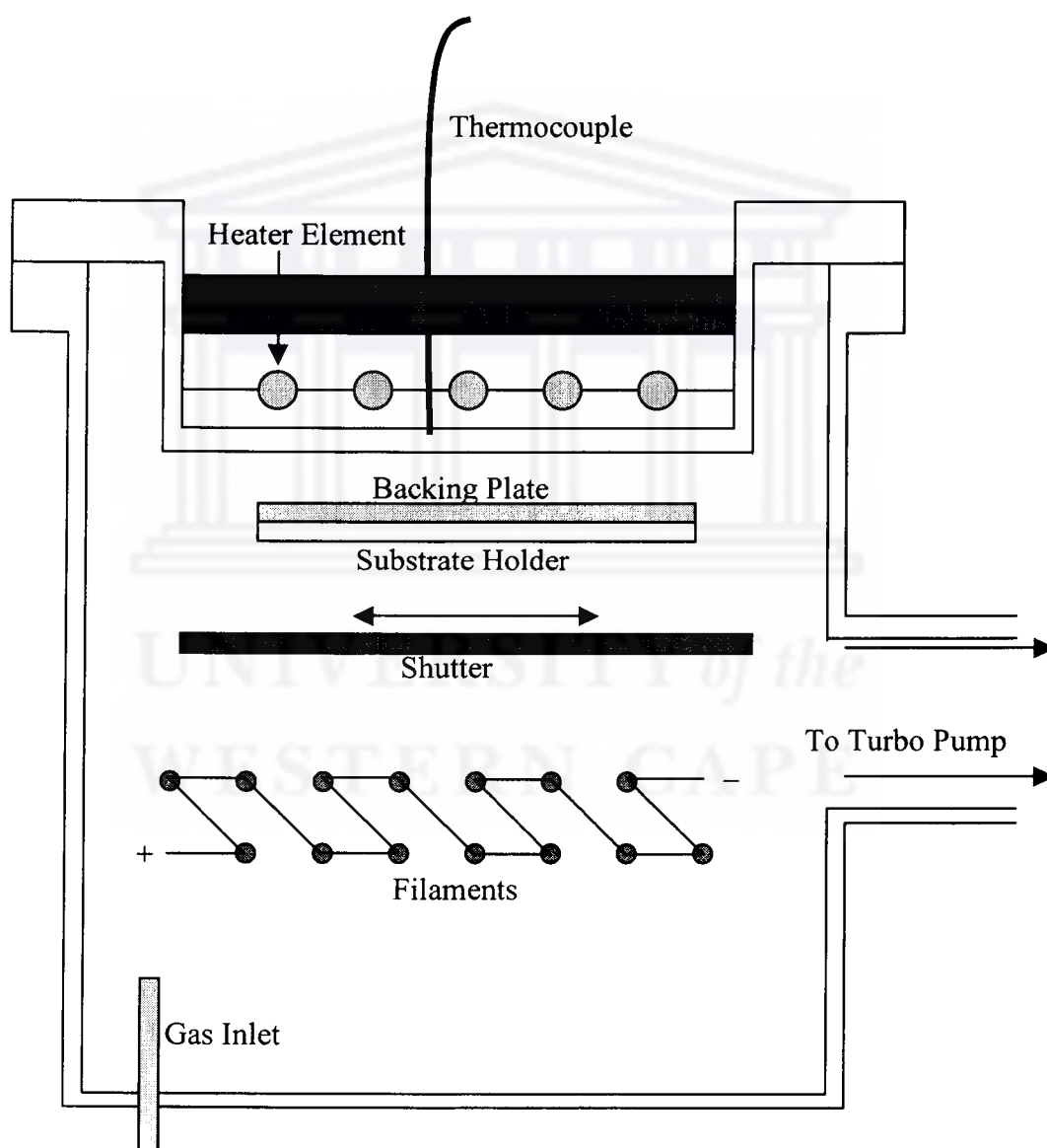
Figure 2.1   Cross-sectional view of the MVSYSTEMS hot-wire reaction chamber.

A shutter reservoir houses a sturdy shutter, which is used to protect the substrate until the proper deposition parameters are attained and to control the deposition exposure time. The shutter is moved in and out of the chamber by using a sliding magnet manipulator between the outer and inner magnet stops. Seven parallel tantalum (Ta) filaments, separated 15 mm apart, are supported on a removable base plate, which includes a power feedthrough and a type K thermocouple feedthrough for reference. The diameter of the Ta wires amounts to 0.25 mm. The distance between the substrate holder and the filament amounts to 18 mm. The temperature of the filament is directly measured by an optical pyrometer. All the components are mounted on a sturdy steel frame that can be moved to alternate locations if desired. The equipment requires a 3 phase 280 V power supply with a 50 A circuit breaker.

2.2.2 SUBSTRATE TEMPERATURE CALIBRATION

The substrate temperature is one of the most important deposition parameters that determines the eventual structure and quality of the deposited a-Si:H film. Therefore it is of utmost importance that the substrate temperature is calibrated with the effects of both the substrate heater and filament temperatures. Figure 2.2 shows the plot of the stabilized substrate temperature versus the heater temperature, with the filament temperature at 1600 °C and the shutter open. The substrate temperature was measured with the thermocouple mounted on a crystalline silicon substrate. The measurements were performed with both the filament and heater temperatures stabilised. The heat transfer between the heater, filament and the substrate is by radiation only. At low heater temperatures the contribution of the filament temperature to the substrate temperature is more than that of the heater temperature. The relation between the substrate temperature $T_{substrate}$ and the heater temperature T_{heater}, for 150 °C $\leq T_{heater} \leq$ 550 °C, and the filament at 1600 °C can be described by the following fitted polynomial:

$$T_{substrate} = 4.07 \times 10^{-4} T_{heater}^2 + 0.514 T_{heater} + 103.68 \qquad (2.1)$$
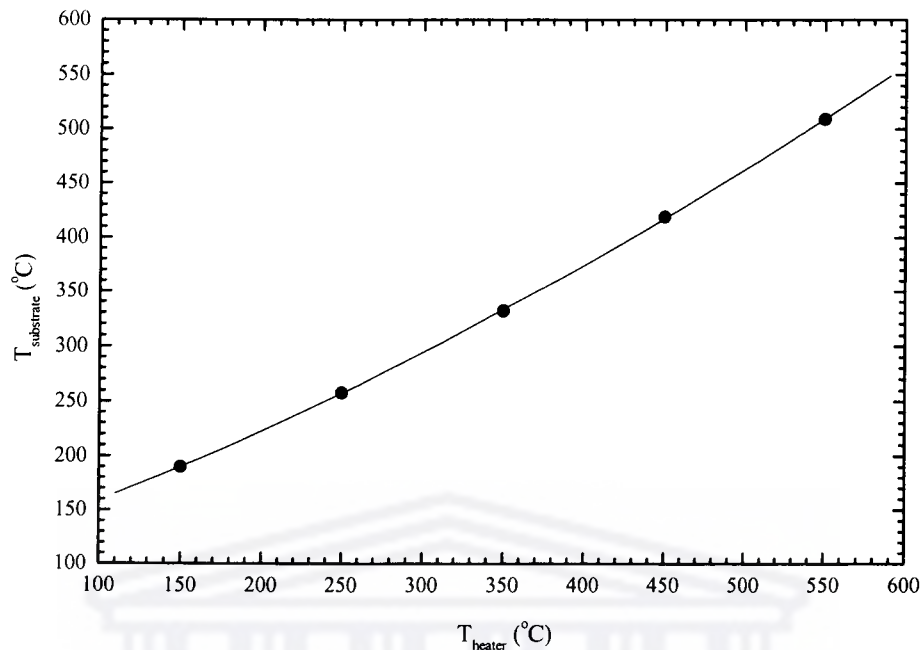
Figure 2.2   Substrate temperature versus heater temperature for $T_{fil} = 1600\ °C$.

2.2.3 SUBSTRATE PREPARATION

The a-Si:H films were simultaneously deposited on the following substrates: single-side polished <100> crystalline silicon (20-30 Ω/cm) and Corning 7059 glass. This allows for various characterisation techniques. Before deposition, the substrates were ultrasonically cleaned with organic solvents to rid their surfaces from impurities. The cleaning sequence was as follows: 5 minutes in acetone followed by 5 minutes in methanol. The substrates were then washed in deionised water to remove any traces of the solvents. The adhesion of the films on the Corning 7059-glass substrate is found to be sufficient. However, the adhesion of the films on the c-Si substrate is quite poor and is enhanced by a subsequent etching in a 5 % HF-solution for about one minute. After drying the substrates, they were mounted onto a rectangular stainless steel substrate holder, which can accommodate both the substrates, each having an area of $25 \times 25\ \text{mm}^2$.

2.2.4 GAS SUPPLY

Seven different gases can be supplied to the reaction chamber: argon (Ar), nitrogen (N_2), silane (SiH_4), hydrogen (H_2), phosphine (PH_3), diborane (B_2H_6) and methane (CH_4). These gases are supplied by a gas system consisting of a supply, exhaust, solenoid valves that are normally closed, manual valves and mass flow controllers. Figure 2.3 shows a schematic representation of the gas supply to the reaction chamber.

The gas supply units are connected to the different gas bottles through Matheson pressure regulators. The gas flows via the mass flow controllers to the reaction chamber and out via the exhaust, which is situated at an elevated position. The gas line connections to the reaction chamber are controlled with high vacuum pneumatic valves that are normally closed, controlled from a separate set of solenoid air pressure valves. A Leybold Trivac B rotary-vane pump with a pumping speed 40 m^3/h is used to pump the exhaust.

Ar or N_2 is used to purge the gas lines and the reaction chamber before or after each deposition run and when a gas bottle is changed. For the deposition of undoped a-Si:H films pure or diluted SiH_4 in H_2 is used. PH_3 and B_2H_6 are used for n- and p-type doping respectively. A maximum flow rate of 100 sccm* can be passed by the mass flow controllers, except for the PH_3 and B_2H_6 controllers, which have maximum flow rates of 10 sccm*.

---

* sccm ≡ standard cubic centimetre per minute

1 sccm = $V_m^{-1} \times 10^{-6}$ m^3/60s ~ 7.440 × 10^{-7} mols^{-1}
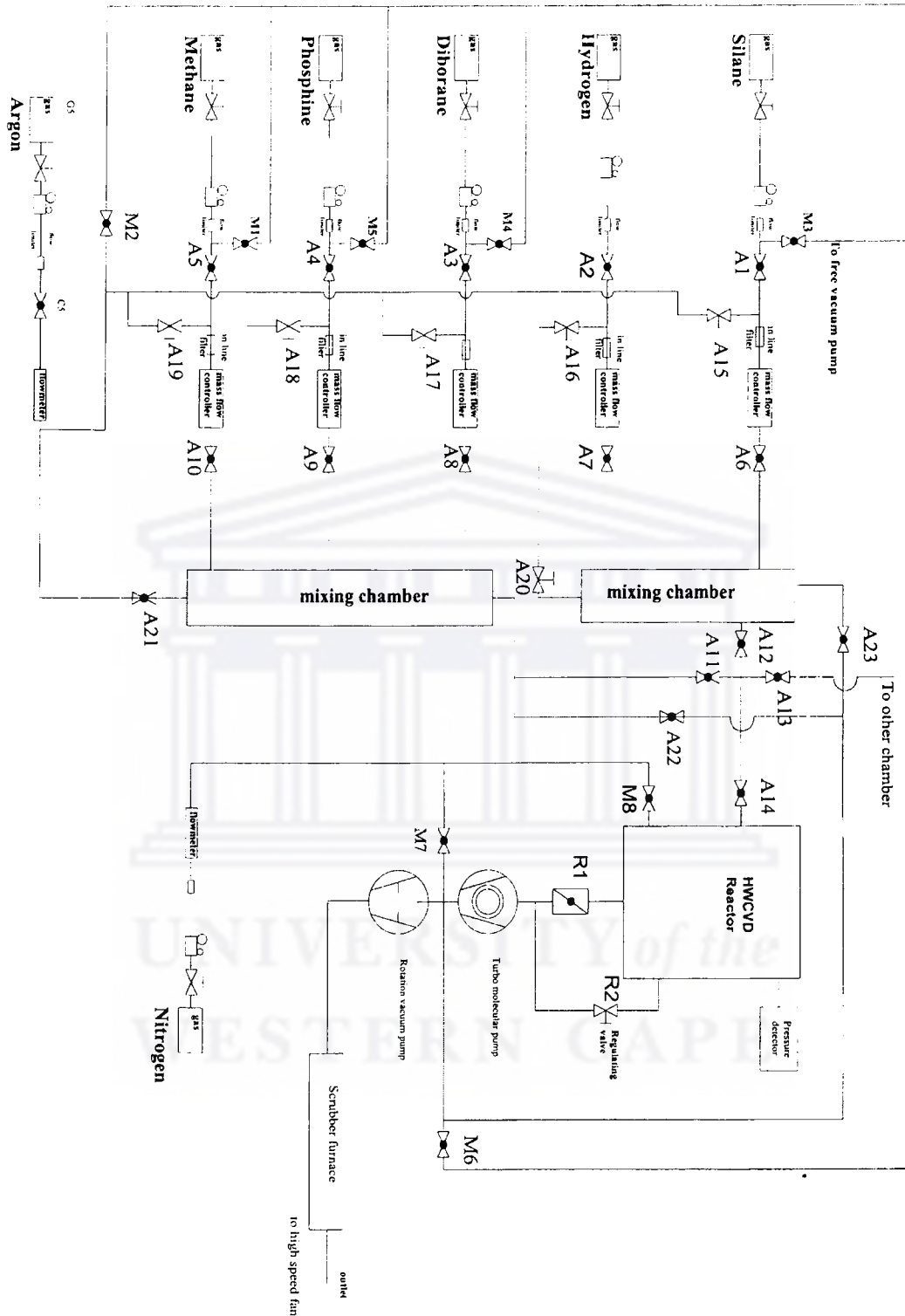
Figure 2.3 Schematic representation of the gas supply to the reaction chamber.

19

2.3 POSITRON ANNIHILATION

2.3.1 INTRODUCTION

Positron annihilation is non-destructive and about the best technique for probing the defect structure in solids, e.g. vacancies and vacancy-type defects. Shultz and Lynn [2.3] have given a review of positron annihilation techniques in solid state applications, which include studies on amorphous silicon. In this thesis we have used Doppler-broadening measurements to study the defect structure of a-Si:H.

2.3.2 THEORY

In dense materials a positron, β^+, which has a vacuum-lifetime of $\sim 2 \times 10^{21}$ a, rapidly thermalises and annihilates with an electron, e^-, predominantly via a two-photon process:

$$\beta^+ + e^- \longrightarrow 2\gamma \qquad (2.2)$$

The thermalization occurs by phonon excitation on a time scale of ~ 10 ps and the annihilation within ~ 1 ns. The energy of each photon amounts to approximately $m_e c^2 = 511$ keV.

The exact energies of the photons depend on $\mathbf{p}$, the total momentum of the positron-electron pair in the laboratory frame, as illustrated in Figure 2.4. In the centre-of-mass frame the photon emission is exactly collinear, as shown by the dashed vectors. If $\mathbf{p}_t$, the transverse component of $\mathbf{p}$, is non-zero, the photon momenta in the laboratory frame are no longer at a 180° angle, as indicated by the solid vectors. While the deviation from collinearity, Φ, depends on the magnitude of $\mathbf{p}_t$; the size of the longitudinal component $\mathbf{p}_l$ determines the energy shifts of the photons.

For non-relativistic electrons ($p \ll m_e c$) the photon energies observed in the laboratory frame are $m_e c^2 - \Delta E$ and $m_e c^2 + \Delta E$, where:

$$\Delta E = \frac{c p_l}{2} \qquad (2.3)$$

and;

$$\Phi = \frac{p_t}{m_e c} \qquad (2.4)$$

The Doppler-broadening technique is essentially a measurement of the distribution of ΔE, whereas the measurement of Φ is referred to as two-dimensional angular correlation of annihilation radiation (2D-ACAR). In this study we focus our attention on Doppler-broadening measurements to study the positron trapping sites in a-Si:H, e.g. voids.
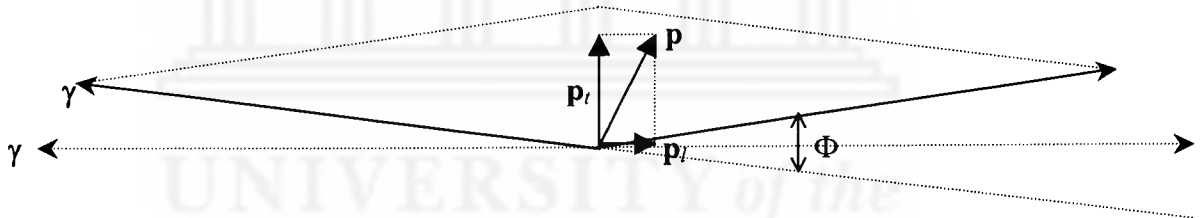
Figure 2.4   Conservation of momentum for annihilation into two photons of an electron-positron pair with total momentum **p**. The vectors **p**$_l$ and **p**$_t$ are the longitudinal and transverse components of **p**, respectively. Dashed vectors represent the collinear photon emission in the centre-of-mass frame. The solid vectors are the photon momenta in the laboratory frame, where a deviation Φ from collinearity is observed. The magnitude of **p** is not to scale.

21

For a particular implantation energy E the slowing down process, which is due to multiple scattering of the positrons in the solid, produces an implantation profile $P(z,E)$ [2.4] that is given by:

$$P(z,E) = -\frac{d}{dz}\exp\left[-\left(\frac{z}{z_o}\right)^m\right]$$ (2.5)

The range parameter, z_o, has an energy dependence and is given by:

$$z_o = \frac{\alpha}{\rho\,\Gamma(1+1/m)}E^n$$ (2.6)

where ρ is the mass density of the sample and Γ is the gamma function.

Widely accepted empirical values [2.5] for the parameters in the positron profile are

$\alpha = 4.0\ \mu g\ cm^{-2}\ keV^{-n}$, m =2 and n = 1.6. Figure 2.5 shows the implantation profile for positrons in crystalline silicon. By varying the positron beam energy, it is possible to vary the implantation depth of the positrons before annihilation. Hence, it is possible to analyse the defect structure of the sample as a function of depth. The mean, $\bar{z}$, and median, $z_{1/2}$, penetration depths are given by:

$$\bar{z} = z_o\frac{\sqrt{\pi}}{2}$$ (2.7)

and;

$$z_{1/2} = z_o\sqrt{\ln 2}$$ (2.8)

For crystalline silicon: $\bar{z}_5 = 0.228\ \mu m$, $\bar{z}_{10} = 0.692\ \mu m$, $\bar{z}_{15} = 1.325\ \mu m$ and $\bar{z}_{20} = 2.099\ \mu m$, as illustrated in Figure 2.5.
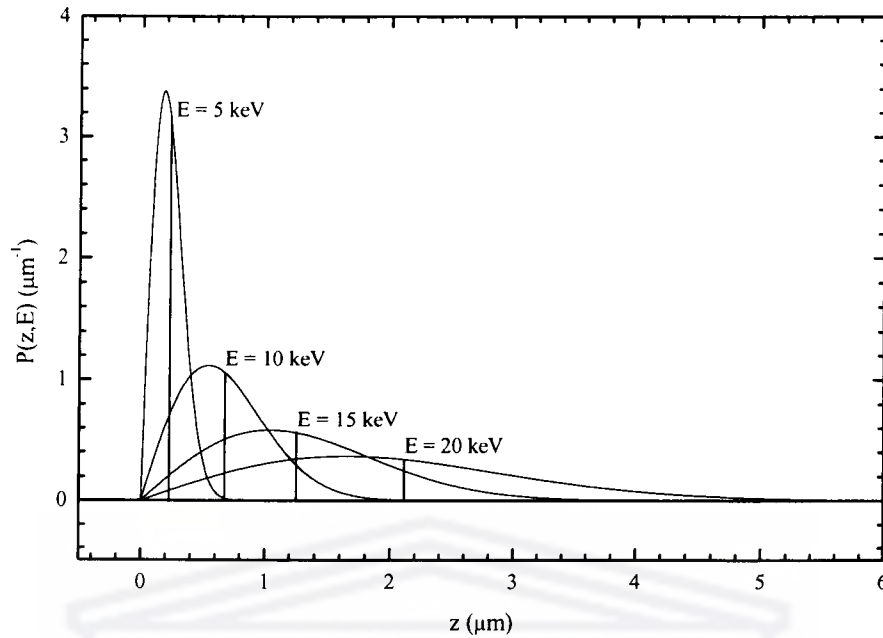
Figure 2.5 Implantation profile for positrons in crystalline silicon calculated for incident positron energies of 5 keV, 10 keV, 15 keV and 20 keV according to equation (2.5).

At a positron beam energy corresponding to the mid-point between the film and the interface the median implantation depth is equal to the film thickness, d. Hence, it is possible to determine the mass density of the sample by measuring the thickness of the film from an independent technique; e.g. using a profilometer. From equations (2.6) and (2.8) it follows that the mass density of the film is given by:

$$\rho = \frac{\alpha\sqrt{\ln 2}}{d \ \Gamma(1+1/m)} E_{1/2}^{n} \qquad (2.9)$$

Mahan *et al.* [2.6] have measured the bulk density of amorphous silicon and found that $\rho_b = 2.270$ g cm^{-3}, which is slightly lower than that of crystalline silicon [2.7]. Thus, by comparing the density of the a-Si:H sample to ρ_b one can obtain information on the void fraction in the sample.

2.3.3 BEHAVIOUR OF POSITRONS IN SOLIDS

FREE AND TRAPPED POSITRONS

Both free and trapped positrons contribute to the Doppler-broadening of the 511 keV-peak in different ways. A free positron can annihilate with both core and conduction electrons, whereas a trapped positron in a vacancy has a relatively small overlap with core electrons. Therefore a trapped positron has a larger probability to annihilate with conduction electrons, which have energies lower than that of core electrons. This results in a reduction of the Doppler-broadening. Therefore the component of the 511 keV-peak that is due to free positron annihilation is wider than that of the trapped positron.

THE POSITRONIUM

A thermal positron can bind to an electron to form a metastable hydrogen-like bound state, called the positronium (Ps). It is assumed that the Ps can only be formed in voids [2.8], since it has not been detected in dense semiconductors. The predominant mode of decay and lifetime of the Ps ground state depend on its spin. The singlet state, $^1S_0$, occurs when the spin is zero, called the para-positronium (p-Ps). The p-Ps, with vacuum lifetime of 125 ps, decays predominantly via a two-photon process. The triplet state, $^3S_1$, occurs when the spin is one, called the ortho-positronium (o-Ps). The o-Ps, with vacuum lifetime of 142 ns, decays predominantly via a three-photon process. Thus the photons emitted during annihilation can have any energy between 0 and 511 keV. The ratio of p-Ps to o-Ps formed, p-Ps: o-Ps = 1:3.

2.3.4 EXPERIMENTAL SET-UP

The positron annihilation experiments were performed using the continuous slow positron beam at the University of Cape Town in Cape Town, South Africa [2.9]. Positrons are created by β^+-decay of an encapsulated ^{22}Na-source, with half-life $t_{\frac{1}{2}}$ = 2.6 a, moderated through a 1 μm-thick tungsten mesh, by the reaction:

$$^{22}\text{Na} \xrightarrow{\quad 2.6\,a \quad} {}^{22}\text{Ne} + \beta^+ + \gamma \qquad (2.10)$$
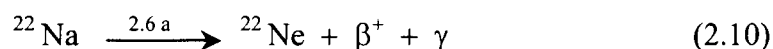
The moderated positrons are preaccelerated to an energy of 250 eV in a vacuum beam line, with a base pressure of 2×10^{-6} Pa, and guided by an axial magnetic field. The positrons are subsequently accelerated to an energy between 0 and 16.3 keV towards the sample, which is secured to the sample holder by silver paste. A type K thermocouple is used to measure the temperature at the sample surface. Six measurement runs were performed at all energies with a total collection time of 300 seconds for each run. After annihilation occurs one of the γ-rays is detected by a liquid nitrogen cooled high-resolution Germanium detector. The measured curve is that of the Doppler-broadening of the 511 keV-peak.

2.4 RAMAN SCATTERING

2.4.1 INTRODUCTION

Raman scattering is the technique most frequently used to study the structural order of a-Si:H, because it is extremely sensitive to minute changes in the short-range order and its non-destructive nature. In particular, Raman scattering can be used to detect any crystalline phases in a-Si:H and to calculate the crystalline fraction in microcrystalline material (μc-Si:H).

2.4.2 THEORY

The Raman effect arises when a beam of intense monochromatic radiation passes through a sample that contains molecules that undergo a change in molecular polarizability as they vibrate [2.10]. In the first-order Raman scattering process, a photon with frequency ω_0 is scattered inelastically by the sample, with the creation or the annihilation of a phonon with frequency ω. Stokes scattering occurs through the creation of a phonon; and after the scattering the photon has frequency $\omega_0 - \omega$. On the other hand, anti-Stokes scattering occurs through the annihilation of a phonon; and after the scattering the photon has frequency $\omega_0 + \omega$.

The Stokes first-order scattering intensity, $I(\omega)$, for amorphous materials is given by [2.11]:

$$I(\omega) = C(\omega)g(\omega)\left(\frac{n_{BE}(\omega) + 1}{\omega} \right) \qquad (2.11)$$

where; $C(\omega)$ is the coupling parameter which represent the polarizability of the phonon modes;

$g(\omega)$ is the phonon density of states; and

$n_{BE}(\omega)$ is the Bose-Einstein thermal factor.

The Bose-Einstein thermal factor is given by:

$$n_{BE}(\omega) = \frac{1}{\exp(\hbar\omega/k_B T) - 1} \qquad (2.12)$$

where k_B is Boltzmann's constant and T the sample temperature.

In c-Si, conservation of crystal momentum requires that $\vec{k} = 0$. This results in a sharp, narrow peak at ~ 520 cm^{-1} in the Raman spectrum [2.12]. The absence of this peak verifies that there is no crystallinity present in the film. In a-Si the network disorder relaxes the k-selection rules and a broad transverse-optical (TO)

band centred at ~ 480 cm^{-1} becomes visible, which reflects the degree of disorder in the amorphous network and can be related to the average bond-angle variation [4.13].

2.4.3 EXPERIMENTAL SET-UP

The Raman scattering measurements were performed on samples deposited on Corning 7059 substrates in backscattering geometry (Debye Institute, Utrecht University) [2.14 – 2.15]. The measurements were performed using the 514.5 nm line of a Spectra Physics Ar$^+$-ion laser. Various optical lenses were used to focus the beam onto the sample. A Spex triple-grating monochromator was used to disperse the scattered light onto a liquid-nitrogen cooled EG&G CCD detector. The frequency shifts were calibrated using Rubidium emission lines. The phonon spectrum was measured in the region 0 – 1000 cm^{-1}.

2.5 OPTICAL MEASUREMENTS

The optical properties of the a-Si:H samples were determined from transmission and reflection measurements in the energy range from 1.2 – 2.4 eV, with an energy resolution of 3 meV (Debye Institute, Utrecht University). The thickness of the film is determined by an iterative procedure, thereby calculating the complex refractive index, $\bar{n} = n + ik$, as a function of energy. The computer code OPTICS [2.16] was used to extract the values for the thickness and refractive index. The refractive index at zero energy n_0 is determined by extrapolating $1/[n^2(E)-1]$ versus E^2 to $E = 0$. The absorption coefficient $\alpha(E)$ is calculated from the imaginary part of the refractive index $k(E)$ by:

$$\alpha(E) = \frac{4\pi k(E)}{\lambda} \tag{2.13}$$

where λ is the wavelength of the incident radiation.

27

The optical band gap E_g can be calculated from the real part of the refractive index n(E) and the absorption coefficient by the following equation:

$$[\alpha(E)n(E)E]^{1\ (1+p+q)} = B_g[E - E_g]$$ (2.14)

The parameters p and q describe the density of states (DOS) distribution of the band edges. If the DOS distribution is taken to be parabolic in both the valence and conduction bands, i.e. for p = q = ½, then equation (2.14) describes the Tauc plot [2.17]. The Tauc band gap is determined by extrapolating $[\alpha(E)n(E)E]^{1/2}$ versus E to $\alpha(E) = 0$; for $\alpha(E) \geq 10^3$ cm^{-1}. If the DOS distribution is taken to be linear, i.e. for p = q = 1, then equation (2.14) describes the Cubic (or Bezemer) plot [2.18]. The resulting Cubic band gap is again determined by extrapolating $[\alpha(E)n(E)E]^{1/3}$ versus E to $\alpha(E) = 0$; for $\alpha(E) \geq 10^3$ cm^{-1}.The Cubic gap is 0.1 – 0.2 eV lower that the Tauc gap and is linear over a larger energy range than the Tauc plot. In this thesis, as in most literature, we will use the Tauc-convention.

2.6 FOURIER TRANSFORM INFRARED SPECTROSCOPY

Fourier transform infrared (FTIR) spectroscopy is the most commonly used technique for the determination of the hydrogen concentration and the silicon-hydrogen bonding configuration in a-Si:H, because it is non-destructive and easy to perform. The measurement consists of measuring a transmission spectrum, T(ω), of the film on a c-Si substrate in the energy range 400 – 4000 cm^{-1}, with an energy resolution of 4 cm^{-1}. A background spectrum of the c-Si substrate was collected in order to eliminate the absorption in the c-Si substrate.

The relation between the transmission spectrum and the absorption coefficient $\alpha(\omega)$ is given by:

$$\alpha(\omega) = -\frac{\ln[T(\omega)]}{d} \qquad (2.15)$$

where d is the thickness of the a-Si:H layer.

To eliminate the effects of incoherent and coherent multiple reflections in the films we used the methods proposed by Brodsky *et al.* [2.19] and Langford *et al.* [2.20, 2.22], respectively. Three different vibrational modes can be distinguished for a-Si:H. They are the $Si–H_x$ (for x =1, 2, 3) rocking mode centred at 630 cm^{-1}, the bending mode around 800 – 900 cm^{-1} and the stretching mode around 2000 – 2130 cm^{-1}. The generally accepted assignments of the $Si–H_x$ vibrational modes to absorption bands are summarised in Table 2.1 [2.21].

Table 2.1 The generally accepted assignments of the $Si–H_x$ vibrational modes to absorption bands [2.21].

Energy (cm^{-1})	Bonding Configuration	Vibrational Mode
630	$\equiv Si–H$, $(=Si=H_2)_n$ for n≥1, $–Si\equiv H_3$	Rocking
845	$(=Si=H_2)_n$ for n≥2	Bending
880	$=Si=H_2$	Bending
890	$(=Si=H_2)_n$ for n≥2	Bending
2000	$\equiv Si–H$ (isolated)	Stretching
2070 – 2100	$\equiv Si–H$ (on voids), $(=Si=H_2)_n$ for n≥1	Stretching
2130	$–Si\equiv H_3$	Stretching

The integrated absorption I_ω of each mode ω is given by:

$$I_\omega = \int_{-\infty}^{+\infty} \frac{\alpha(\omega)}{\omega_0} d\omega \qquad (2.16)$$

The concentration of bonded hydrogen C_H is proportional to I_ω via:

$$C_H = A_\omega I_\omega \qquad (2.17)$$

where A_ω is the proportionality constant which depends on the oscillator strength of the Si–H bonds. The constant A has been determined empirically with independent techniques, such as elastic recoil detection (ERD) and nuclear reaction analysis (NRA) [2.22 – 2.25]. From FTIR spectroscopy it is also possible to obtain information on the microstructure in a-Si:H. The 2000 cm^{-1} mode is caused by $\equiv$Si–H bonds, while the 2070 – 2100 cm^{-1} mode is caused by hydrogen bonded in various forms of microstructure; i.e. =Si=H_2 units, (=Si=H_2)$_n$ polyhydrides for n$\geq$2 and $\equiv$Si–H on void surfaces. Therefore, the microstructure parameter R^* is a measure of the structural quality of a-Si:H, and is given by:

$$R^* = \frac{I_{2070}}{I_{2000} + I_{2070}} \qquad (2.18)$$

Device quality a-Si:H films have R^*-values that are typically not larger than 0.1.

2.7 ELASTIC RECOIL DETECTION

2.7.1 INTRODUCTION

Elastic Recoil Detection (ERD) or Forward Recoil Spectrometry (FRES), which was first introduced by L'Ecuyer *et al.* [2.26], is one of the most useful non-destructive ion-beam analysis techniques for easy depth profiling of light elements. ERD can be used to determine hydrogen and deuterium concentration depth profiles in solids to depths of a few microns by using $^4He^+$ ions at energies of a few MeV.

2.7.2 THEORY

ERD, like Rutherford Backscattering Spectrometry (RBS) [2.27 – 2.28], is based on the elastic collision between high-energy ions and the atoms in the sample. The particles that are detected and analysed are the recoils, which are scattered in a forward direction; i.e. particles that are lighter than the incident projectile. The kinematics of the experiment in the laboratory reference frame is shown in Figure 2.6 [2.27].
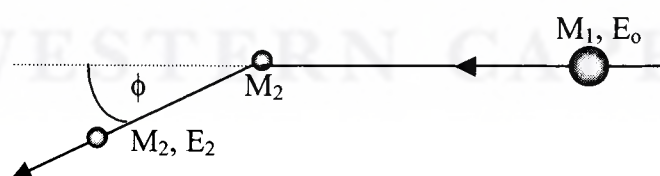
Figure 2.6   Schematic representation of the elastic collision between a projectile of mass M_1 at an energy E_o, and the target mass M_2 which is initially at rest. After the collision the target mass is scattered with an energy E_2 at a scattering angle ϕ

Consider the following situation: a beam of projectiles of mass M_1, atomic number Z_1, at an energy E_o is incident upon a sample. The recoiled atom of mass M_2, atomic number Z_2, is scattered with an energy E_2 at an angle ϕ. The energy of the recoiled atom can be related to the projectile energy by the kinematic factor [2.27 – 2.28], K, such that:

$$E_2 = KE_o \tag{2.19}$$

where;

$$K = \frac{4M_1M_2}{(M_1 + M_2)^2}\cos^2\phi \tag{2.20}$$

From equation (2.20) it is clear that the kinematic factor K depends on the scattering angle ϕ, the projectile mass M_1 and recoiled mass M_2. If the ratio E_2/E_o, the projectile mass and the scattering angle are known, the recoiled mass can be determined. Thus from the kinematic factor it is possible to identify which atoms are present in the sample.

Another important characteristic for the elastic collision is the probability with which it takes place. The chance that one particle from the projectile beam ejects a recoil atom in such a way that it is recoiled in the direction of the detector is described by the Rutherford differential cross section, which is governed by coulombic scattering. The differential cross section is given by [2.27 – 2.28]:

$$\frac{d\sigma}{d\Omega} = \left(\frac{Z_1Z_2e^2(1 + M_1/M_2)}{2E_o}\right)^2 \frac{1}{\cos^3\phi} \tag{2.21}$$

where Ω is the finite solid angle spanned by the detector, and e is the electron charge.

For a constant concentration of target atoms, the yield or the number of detected particles is related to the number of target atoms/cm^2 by the following equation [2.27 – 2.28]:

$$Y = Q\Omega N_s \int_0^{E_o} \frac{d\sigma}{d\Omega}(E,\phi)\left(\frac{dE}{dx}\right)^{-1} dE \qquad (2.22)$$

2.7.3 EXPERIMENTAL SET-UP

ERD measurements were performed on samples deposited on c-Si substrates at the Materials Research Group of *i*Themba Labs at Faure, South Africa [2.2]. A schematic representation of the experimental set-up for ERD measurements is shown in Figure 2.7.
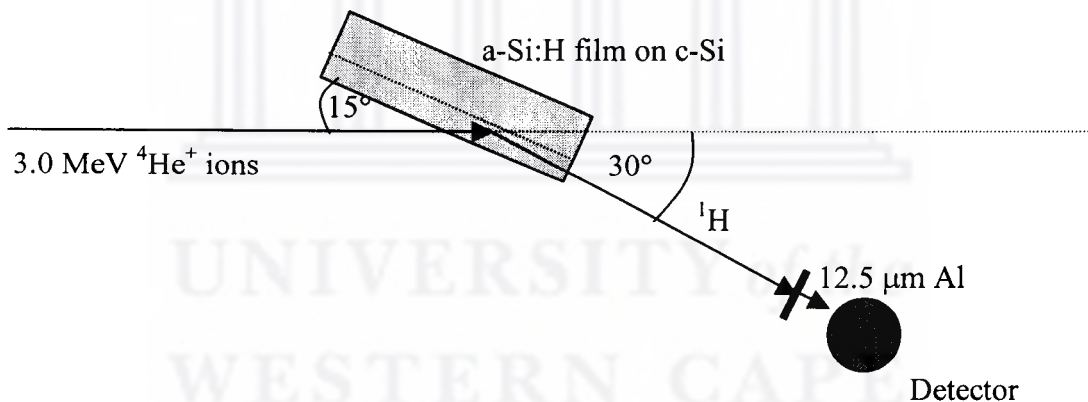
Figure 2.7   Schematic representation of the ERD experimental set-up.

The samples were analysed using a 3.0 MeV mono-energetic and collimated beam of ^{4}He$^+$ ions, which were accelerated by a van de Graaff accelerator. A vacuum of approximately 10^{-6} Pa was achieved and maintained in the ERD chamber by using a fore pump and a turbo molecular pump. The sample holder was rotated at an angle of 15° with respect to the direction of the incident projectile beam. The recoiled atoms were detected at an angle of 30° with respect to the direction of the incident projectile beam. An aluminium foil of thickness 12.5 μm was used to

prevent the scattered primary $^4\text{He}^+$ ions from reaching the solid state detector, which is mounted in the plane of the beam. The solid state detector generates an electronic signal which was amplified and processed using analogue and digital electronics. They are sorted according to pulse height (energy) and stored in a multi-channel analyser. Before each measuring session a reference spectrum of a mylar ($C_{10}H_8O_4$) foil was collected which was then used for the energy and geometry calibration.

34

REFERENCES

[2.1] MVSystems Inc., in "Operating Manual for the Hot-Wire CVD System, Version 1.0", Physics Department, University of the Western Cape, Bellville, South Africa (1997)

[2.2] C. J. Arendse, in "Hydrogenated Amorphous Silicon: Optical Properties and Hydrogen Concentration", M.Sc. thesis, University of the Western Cape, Bellville, South Africa (1999)

[2.3] P. J. Schulz and K. G. Lynn, Rev. Mod. Phys. **60** (1998) 701

[2.4] S. Valkealahti and R. M. Nieminen, Appl. Phys. **A 32** (1983) 95

[2.5] A. Vehanen, K. Saarinen, P. Hautojärvi and H. Huomo, Phys. Rev. **B 35** (1987) 4606

[2.6] A. H. Mahan, D. L. Williamson, B. P. Nelson and R. S. Crandall, Sol. Cells **27** (1989) 465

[2.7] M. Levinshtein, S. Rumyantsev and M. Shur (eds.), in "Handbook Series on Semiconductor Parameters Vol. I", World Scientific, Singapore (1996)

[2.8] Y. J. He, M. Hasegawa, R. Lee, S. Berko, D. Adler and A. L. Jung, Phys. Rev. **B 33** (1986) 5924

[2.9] D. T. Britton, M Härting, M. R. B. Teemane, S. Mills, F. M. Nortier and T. N. van der Walt, Appl. Surf. Sci. **116** (1997) 53

[2.10] H. H. Willard, L. L. Merritt Jr., J. A. Dean and F. A. Settle Jr., in "Instrumental Methods of Analysis 7th Edition", Wadsworth Publ. Co. (1988)

[2.11] F. L. Galeener and P. N. Sen, Phys. Rev. **B 17** (1978) 1928

[2.12] P. A. Temple and C. E. Hathaway, Phys. Rev. **B 7** (1973) 3685

[2.13] D. Beeman, R. Tsu and M. F. Thorpe, Phys. Rev. **B 32** (1985) 874

[2.14] A. J. M. Berntsen, in "Structural Disorder in Pure and Hydrogenated Amorphous Silicon", Ph.D. thesis, Utrecht University, Utrecht, The Netherlands (1993)

[2.15] A. M. Brockhoff, in "Hydrogen-Related Modifications of Amorphous Silicon and Silicon Nitride", Ph.D. thesis, Utrecht University, Utrecht, The Netherlands (2001)

[2.16]   M. J. van den Boogaard, in "Microvoids and Hydrogen Diffusion in Hydrogenated Amorphous Silicon", Ph.D. thesis, Utrecht University, Utrecht, The Netherlands (1992)

[2.17]   J. Tauc, in "Optical Properties of Solids", ed. F. Abeles, North-Holland Publ., Amsterdam (1972)

[2.18]   R. H. Klazes, M. H. L. M. van den Broek, J. Bezemer and S. Radelaar, Phil. Mag. **B 45** (1982) 377

[2.19]   M. H. Brodsky, M. Cardona and J. J. Cuomo, Phys. Rev. **B 16** (1977) 3556

[2.20]   N. Malay, Phys. Rev. **B 46** (1992) 2078

[2.21]   G. Lucovsky, R. J. Nemanich and J. C. Knights, Phys. Rev. **B 19** (1979) 2064

[2.22]   A. A. Langford, M. L. Fleet, B. P. Nelson, W. A. Lanford and N. Malay, Phys. Rev. **B 45** (1992) 13367

[2.23]   C. L. Fang, K. J. Gruntz, L. Ley, M. Cardona, F. J. Demond, G. Muller and S. Kalbitzer, J. Non-Cryst. Solids **35 – 36** (1980) 255

[2.24]   G. Amato, G. Della, F. Fizzotti, C. Manfredotti, R. Marchiso and A. Paccagnella, Phys. Rev. **B 43** (1991) 6627

[2.25]   J. Daye Ouwens, in "Characterization and Application of Wide band Gap Amorphous Silicon", Ph.D. thesis, Utrecht University, Utrecht, The Netherlands (1995)

[2.26]   J. L'Ecuyer, C. Brassard, C. Cardinal, J. Chabbal, L. Deschenes, J. P. Labrie, B. Terreault, J. G. Martel and R. St.-Jacques, J. Appl. Phys. **47** (1976) 381 (1976)

[2.27]   L. C. Feldman and J. W. Mayer, in "Fundamentals of Surface and Thin Film Analysis", North-Holland Publ., Amsterdam (1986)

[2.28]   J. R. Tesmer, M. Nastasi, J. C. Barbour, C. J. Maggiore and J. W. Mayer, in "Handbook of Modern Ion Beam Materials Analysis", Pittsburgh, Pennsylvania (1995)

CHAPTER 3

Hydrogen Bonding

and Migration

3.1 INTRODUCTION

Hydrogenated amorphous silicon (a-Si:H) has proven to be of technological importance and is successfully used in several large-area thin film applications like solar cells and thin film transistors. However one major drawback of a-Si:H, and subsequently devices made from this material, is that the electrical properties degrade under prolonged illumination [3.1]. This effect, known as the Staebler-Wronski effect (SWE), manifests itself in the increase of the mid gap defect density upon illumination, as shown by Hirabayashi *et al.* [3.2] and Dersch *et al.* [3.3]. These defects are metastable and can be reversed by annealing the material at temperatures above 150 °C [3.1].

An impressive amount of work has been done to provide a mechanism of this light-induced defect creation effect and various models have been proposed [3.4 – 3.11, 3.19 – 3.26]. Mahan *et al.* [3.12] reported that HW-deposited a-Si:H with low H-concentrations shows a reduction in the SWE. The microscopic origin of the SWE is still poorly understood, but it has been established that hydrogen plays an active role in the defect creation. However, the role that hydrogen plays and how it

is played is controversial and therefore it is of importance to characterise this hydrogen induced effects in order to enhance the stability of future devices.

In this chapter we report on the effects of isochronal annealing at temperatures ranging from 150 – 450 °C on the infrared (IR) absorption spectra of HW-deposited a-Si:H samples with different H-concentrations and bonding configurations. In particular, we will focus on the influence of the initial H-concentration on the hydrogen bonding and migration.

This chapter is organised as follows. In the next section the experimental details of the sample preparation, heat treatments and characterisation techniques are described. In section 3.3 the difference between isolated and clustered hydrogen is discussed and, in particular, the quantitative data analysis of the IR absorption spectra. The results of hydrogen bonding and migration are discussed in Section 3.4, followed by concluding remarks drawn in Section 3.5.

3.2 EXPERIMENTAL DETAILS

3.2.1 SAMPLE PREPARATION

Two a-Si:H samples, with different H-concentrations, were deposited by hot-wire chemical vapour deposition in the MVSYSTEMS deposition chamber [3.13], where SiH$_4$-gas is decomposed by the catalytic action of seven parallel Ta-wires at a temperature of 1600 ± 50 °C. The samples were deposited simultaneously on Corning 7059 and <100> c-Si substrates to meet the requirements for the different characterisation techniques.

Sample A, with C$_H$ ~ 7 at.%, was deposited at a growth temperature of 330 °C, using 60 sccm SiH$_4$-gas under a pressure of 2 Pa. Sample B, with C$_H$ ~ 11 at.%, was deposited at a growth temperature of 180 °C, using 60 sccm SiH$_4$-gas under a pressure of 8 Pa.

3.2.2 HEAT TREATMENTS

Isochronal thermal treatments were performed under high-purity, flowing argon gas in a tube furnace. The samples were annealed subsequently at annealing temperatures ranging from 150 – 450 °C in 50 °C increments. The total annealing time was 30 minutes for all temperatures.

3.2.3 CHARACTERISATION

FTIR measurements were performed in transmission geometry on films deposited on c-Si substrates. The IR absorption spectra were collected in the energy range 400 – 4000 cm^{-1} with an energy resolution of 4 cm^{-1}, using a DIGILAB FTS-40 Fourier-transform infrared spectrometer with a liquid-nitrogen-cooled HgCdTe detector (Debye Institute, Utrecht University). The ambient temperature in the FTIR set-up amounted to 21 °C.

ERD measurements were used to verify the initial H-concentration of the samples, as calculated from IR absorption spectra, and were found to be within 10 %. Therefore, in the as-deposited state no H_2 is present in both samples. Refer to Section 2.7 for the experimental set-up of the ERD measurements (Materials Research Group, *i*Themba Labs).

Scanning electron microscope images were obtained using a HITACHI X650 scanning electron microscope, equipped with analySIS$^{®}$ imaging software, and capable of operating at a maximum accelerating voltage of 40 kV (Electron Microscope Unit, University of the Western Cape).

3.3 ISOLATED AND CLUSTERED HYDROGEN: DATA ANALYSIS

The most direct characterisation technique used to study the behaviour of hydrogen in a-Si:H is the detection of the changes in the IR absorption spectra caused by annealing effects. The change in the intensity of an absorption peak is associated with a change in the concentration of hydrogen bonded in a particular bonding configuration. Therefore FTIR spectroscopy is the most common used technique to study hydrogen migration and diffusion in a-Si:H and other related materials such as hydrogenated amorphous silicon nitride (a-SiN$_x$:H) and hydrogenated amorphous silicon carbide (a-Si:H:C).

The generally accepted assignments of hydrogen bonding configurations to absorption energies for a-Si:H have been established over the last few decades and are summarised by Lucovsky [3.14] (see Table 2.1). The rocking vibration centred at $\sim$ 640 cm^{-1} is associated with all bonding configurations of hydrogen, whereas the bending vibration in the range 800 – 900 cm^{-1} is associated with (=Si=H$_2$)$_n$ dihydride and polyhydride groups. The 2000 cm^{-1} absorption peak, referred to as the isolated phase, originates from the stretching vibrations of isolated $\equiv$Si–H monohydrides. The stretching mode centred at $\sim$ 2100 cm^{-1}, referred to as the clustered phase, is caused by hydrogen bonded in various forms of microstructure; i.e. (=Si=H$_2$)$_n$ dihydride and polyhydride groups and $\equiv$Si–H monohydrides on void surfaces.

The concentration of bonded hydrogen, C_H, was calculated from the integrated absorption coefficient of the rocking mode at 640 cm^{-1}, I_{640}, using the proportionality constant proposed by Shanks *et al.* [3.15], by:

$$C_H = A_{640} I_{640} \qquad (3.1)$$

.

where $A_{640} = 1.6 \times 10^{19}$ cm^{-2}.

The error in the results is estimated to be within 15 %. We assume that A_{640} is independent of the deposition conditions and/or annealing history. Due to the overlapping of the IR stretching modes, the spectra are deconvoluted assuming a Gaussian shape for all absorption modes. Figure 3.1 shows an example of the IR absorption stretching modes of sample B in the as-deposited state and after annealing at 150 °C.
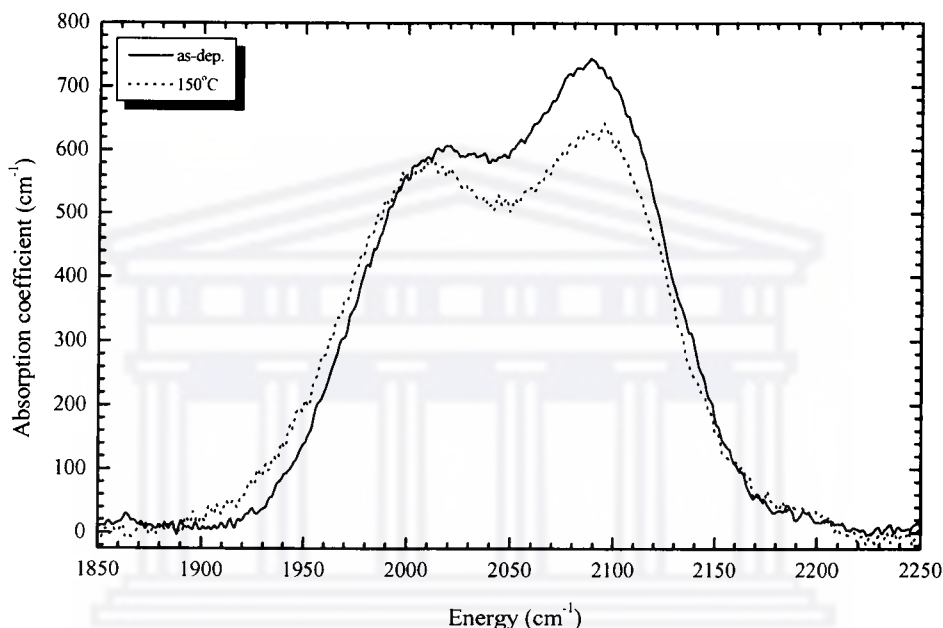
Figure 3.1   Example of the IR absorption stretching modes of sample B in the as-deposited state (solid line) and after annealing at 150 °C (dotted line).

The corresponding deconvolution of the 2000 and 2100 cm^{-1} stretching modes are shown in Figure 3.2. We observe a change in the integrated absorption coefficients of the 2000 and 2100 cm^{-1}-peaks, indicating that hydrogen is transferred from the clustered phase to the isolated phase. This transfer of hydrogen is referred to as hydrogen migration.

41
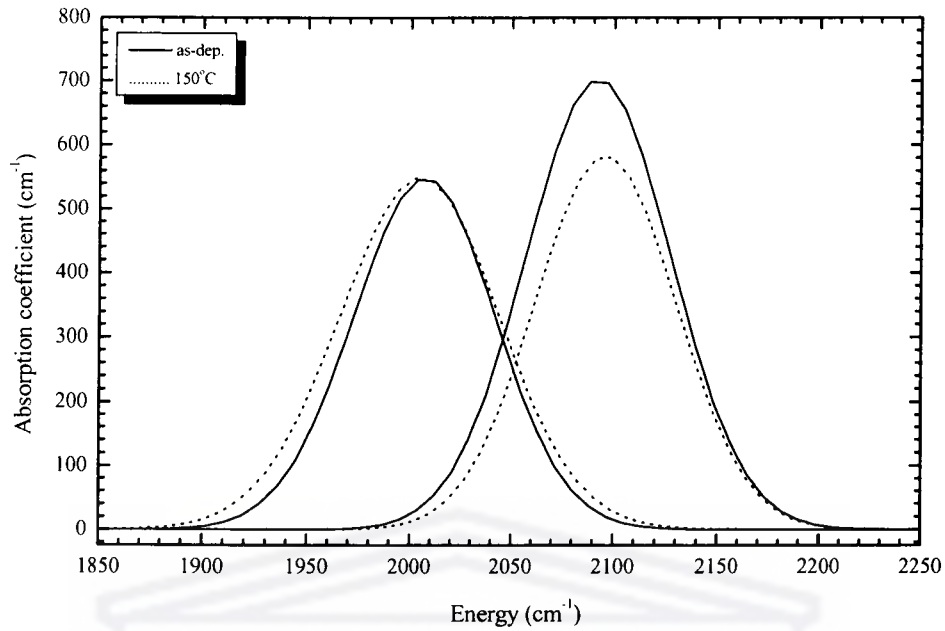
Figure 3.2 Deconvolution of the 2000 and 2100 cm^{-1} stretching modes of sample B (in Figure 3.1) in the as-deposited state (solid line) and after annealing at 150 °C (dotted line).

The concentration of hydrogen bonded in the isolated phase, C_{Hi}, is given by:

$$C_{Hi} = A_{2000} I_{2000} \qquad (3.2)$$

where $A_{2000} = (8.1 \pm 0.9) \times 10^{19}$ cm^{-2} [3.16]. A_{2000} was calculated from IR absorption spectra for device-quality samples with negligible hydrogen bonded in the clustered phase; i.e. for samples where $C_H = C_{Hi}$.

The concentration of hydrogen bonded in the clustered phase, C_{Hc}, is given by:

$$C_{Hc} = A_{2100} I_{2100} \qquad (3.3)$$

Van den Boogaard [3.16] calculated A_{2100} from the difference between C_H and C_{Hi}; i.e. $A_{2100} = (C_H - C_{Hi})/I_{2100}$; and found that $A_{2100} = A_{2000}$.

It is possible to observe the migration of hydrogen to and from void surfaces, since the bending modes are due only to hydrogen bonded in polyhydride configurations. Thus we can estimate the concentration of hydrogen bonded on void surfaces from the integrated absorption coefficients of the bending modes and the stretching mode at 2100 cm^{-1}.

3.4 RESULTS AND DISCUSSION

3.4.1 LOW H-CONCENTRATION: $C_H \sim 7$ at.%

Figure 3.3 shows the temperature evolution of the IR stretching bands for sample A. After annealing the sample at 450 °C the error in the intensity of the stretching band is relatively high, rendering any further calculations pointless. In the as-deposited state the stretching band is symmetrical around $\sim 2000 \text{ cm}^{-1}$, indicating that H is bonded predominantly as $\equiv$Si–H monohydrides.
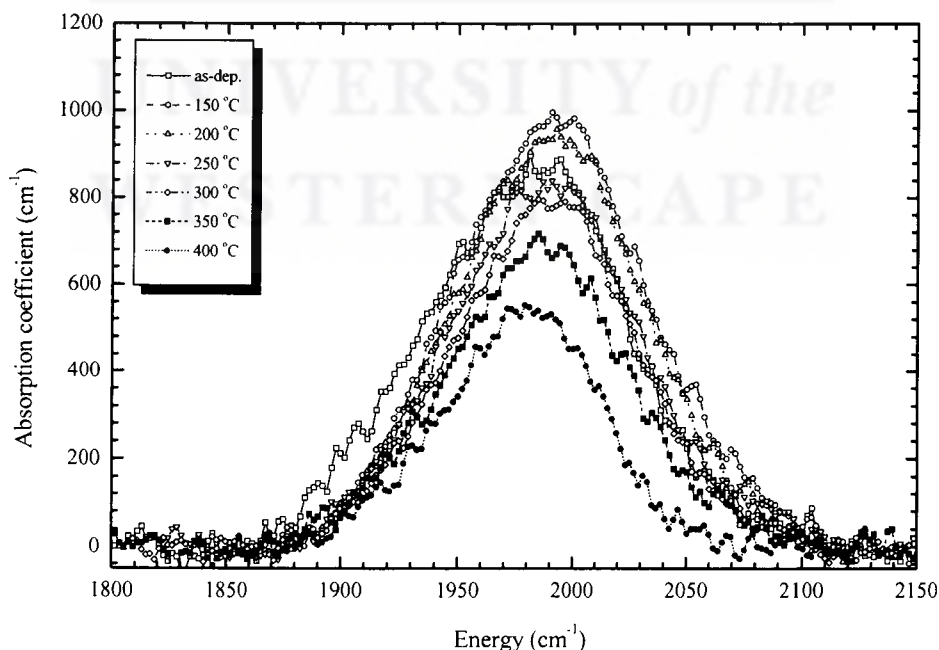
Figure 3.3   Temperature evolution of the IR stretching bands for sample A.

No H migration is observed as annealing progresses, as seen from the continuous symmetrical shape of the stretching band. Figure 3.4 shows the plot of the bonded hydrogen concentration, C_H, and the displacement of the 2000 cm^{-1}-peak position, P_{2000}, as a function of annealing temperature. For $T_A \leq 200$ °C no considerable change in IR absorption spectra, and hence in C_H and P_{2000}, is observed.
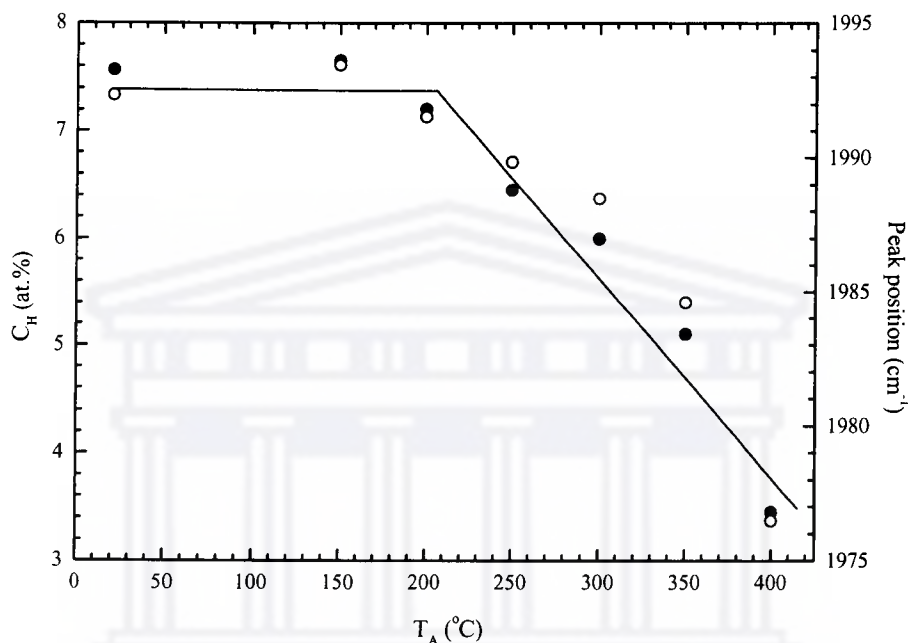
Figure 3.4   Hydrogen concentration (solid circles) and displacement of the 2000 cm^{-1}-peak position (open circles) as a function of annealing temperature for sample A. The line is drawn to guide the eye.

After annealing the sample at $T_A \geq 250$ °C a narrowing and a shift of the 2000 cm^{-1}-peak is observed, suggesting a reduction in the energy distribution of the ≡Si–H bonds. This could arise from H atoms being released from less stable configurations (shallow trapping states), as seen from the reduction in C_H, and consequently leading to H-diffusion [3.17]. In this temperature range a 17 cm^{-1}-decrease in P_{2000} is observed, indicating a reduction in the ≡Si–H bond strength. We attribute the reduction in C_H and P_{2000} primarily to an increase in the network disorder, resulting in H being released from disorder-induced monohydride configurations and thereby reducing the energy cost of breaking the ≡Si–H bond. This is in agreement with the models of Biswas *et al.* [3.22] and Branz [3.5], who

identified the ≡Si–H bond as the original site of hydrogen emission under illumination, resulting in the formation of Si dangling bonds and mobile H and thereby reducing the ≡Si–H bond strength.

3.4.2 HIGH H-CONCENTRATION: $C_H \sim 11$ at.%

Figure 3.5 shows the temperature evolution of the IR stretching bands for sample B. It is evident from this figure that the annealing behaviour of this sample is more complex than that of sample A. The asymmetrical shape of the stretching bands illustrates the relatively large fraction of H bonded in the clustered phase. The IR absorption spectra also show weak bending vibration peaks centred at 845 and 880 cm^{-1} in Figure 3.6, which is typical for HW-deposited a-Si:H with $C_H \sim 11$ at.% [3.18]. As the annealing temperature increases the integrated absorption coefficient of the bending vibration peaks approaches zero at 350 °C. The plots of I_{2000}, I_{2100} and $I_{845} + I_{880}$ as a function of annealing temperature for sample B are given in Figure 3.7. After annealing the sample at 500 °C the error in the intensity of the stretching bands is relatively high, rendering any further calculations pointless.
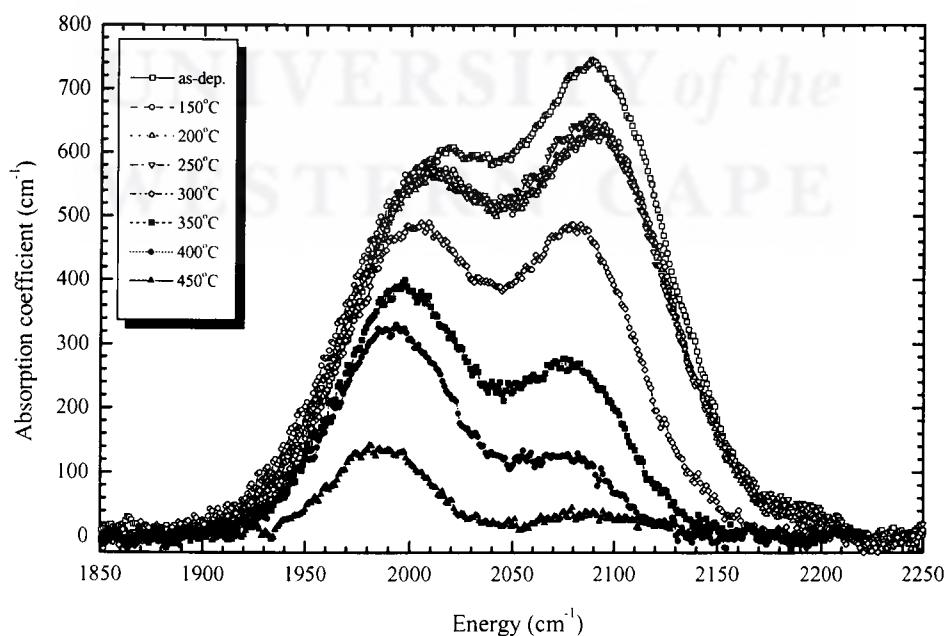
Figure 3.5   Temperature evolution of the IR stretching bands for sample B.
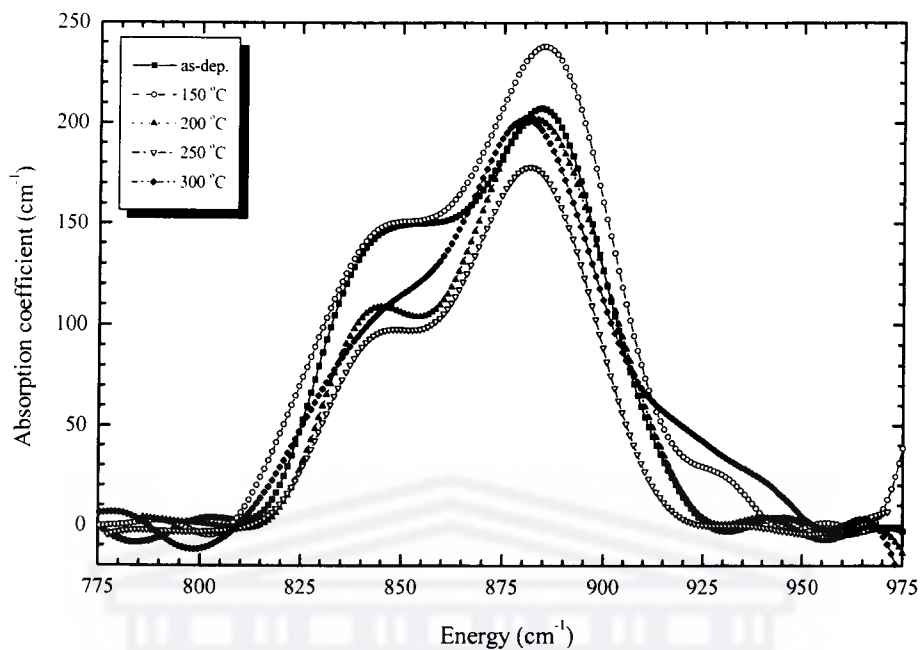
Figure 3.6   Temperature evolution of the IR bending bands for sample B.
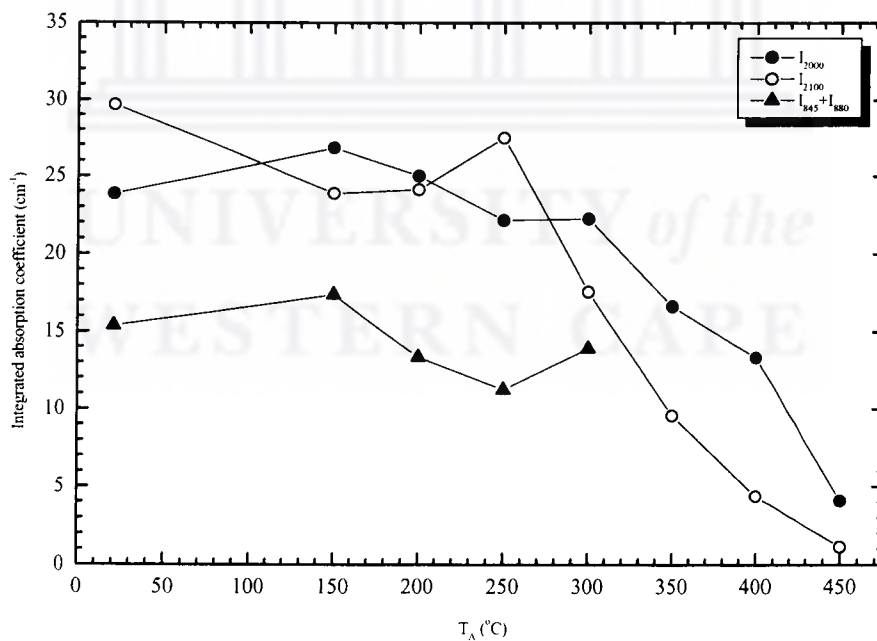
Figure 3.7   Integrated absorption coefficients, I_{2000} (solid circles), I_{2100} (open circles) and $I_{845} + I_{880}$ (solid triangles), as a function of annealing temperature for sample B.

During annealing at $T_A \leq 200$ °C an exchange in I_{2000} and I_{2100} is observed, accompanied by a decrease in $I_{845} + I_{880}$ at 200 °C. In this temperature range no change in C_H is observed, as shown in Figure 3.8. This is indicative of H migrating preferentially from $(=Si=H_2)_n$ polyhydrides to $\equiv Si-H$ monohydrides. Hydrogen bonded in the clustered phase is situated in shallower traps than H bonded in the isolated phase [3.19] and therefore, in this temperature range, H is more readily removed from the clustered phase and settles into a more stable monohydride configuration.
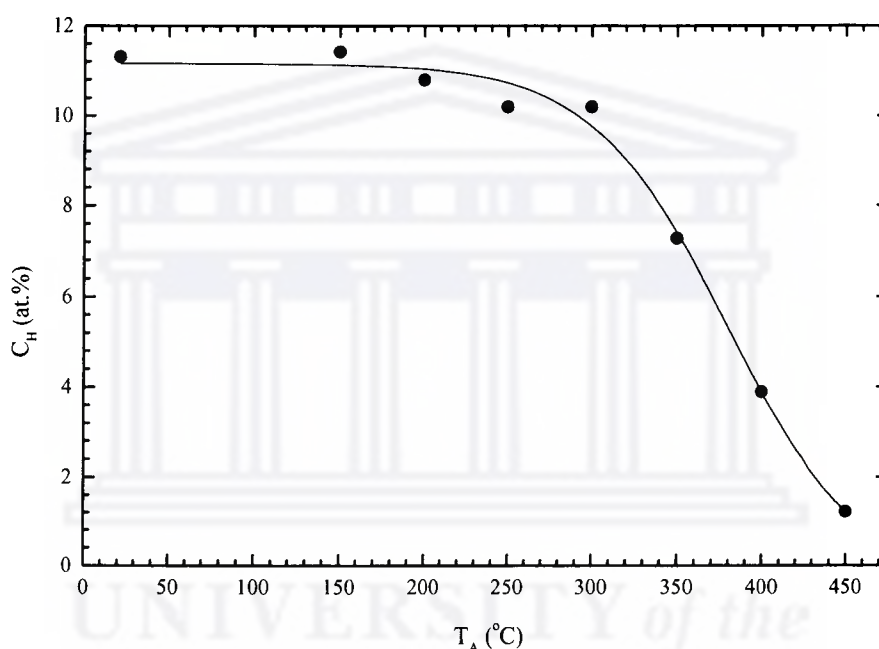
Figure 3.8 Hydrogen concentration as a function of annealing temperature for sample B. The line is drawn to guide the eye.

After the 250 °C anneal an increase in I_{2100} is observed, accompanied by a decrease in I_{2000}. No change in $I_{845} + I_{880}$ and C_H is observed at this temperature outside of the experimental uncertainty, indicating that H is migrating from isolated $\equiv Si-H$ bonds and is likely to be incorporated on the internal surfaces of voids. This implies the following: (a) more bonds on the internal surfaces of the voids are progressively being occupied by hydrogen; and/or (b) there is an increase in the void surface area; and/or (c) there is an increase in the number of voids.

Since no bending vibrations are detected for $T_A \geq 350$ °C, we conclude that the H bonded in the clustered phase is incorporated as $\equiv$Si–H bonds on void surfaces. After annealing the sample at 350 °C H-diffusion, preferentially from the clustered phase, is observed and continues until the initial C_H is reduced by 90 % to 1.22 at.% at 450 °C. We attribute this to an increase in the network disorder, thereby resulting in the preferential removal of H from disorder-induced shallow states; i.e. H bonded on the internal void surfaces.

Figure 3.9 shows the displacement of the 2000 and 2100 cm^{-1} peak positions, P_{2000} and P_{2100}, as a function of annealing temperature. For $T_A \leq 250$ °C no significant changes in the peak positions are observed. In the temperature range 300 – 450 °C, P_{2000} and P_{2100} decrease by ~ 20 cm^{-1} and 13 cm^{-1}, respectively.
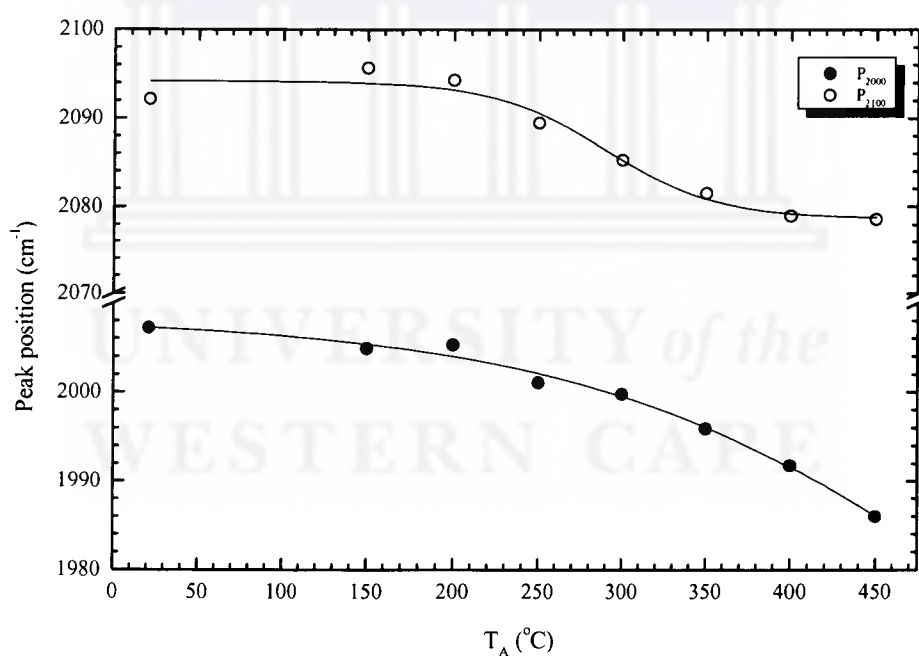
Figure 3.9   Displacement of the 2000 cm^{-1} (solid circles) and 2100 cm^{-1} (open circles) peak positions as a function of annealing temperature for sample B. The lines are drawn to guide the eye.

The reduction in P_{2000} and P_{2100} is indicative of a reduction in the strength of isolated $\equiv$Si–H bonds and $\equiv$Si–H bonds on void surfaces, respectively, and is primarily due to an increased network disorder, as in the case for sample A. This illustrates that the original site of H emission for sample B is a combination of isolated $\equiv$Si–H bonds and $\equiv$Si–H bonds on void surfaces, resulting in the creation of Si dangling bonds and mobile H.

It has been shown that for $T_A > 300$ °C two mobile H atoms recombine and eventually result in H_2 formation [3.20]. Furthermore, these H_2 molecules become trapped in H-rich clusters or voids and are thought to remain stable up to relatively high temperatures [3.21]. It is generally accepted that H out-diffusion occurs via an accumulation of H_2 molecules in high-pressure bubbles, which eventually opens by explosion and consequently results in the blistering of the sample surface [3.21]. Figures 3.10 (a) and (b) show scanning electron micrographs of sample B annealed at 450 °C at a magnification of $\times$ 0.8 k and 1.3 k, respectively. Holes with diameters of ~ 1.5 μm are visible, demonstrating the blistering of the sample surface. Similar observation were observed for H_2^+-implanted a-Si [3.21] and plasma-deposited a-Si:H [3.27].
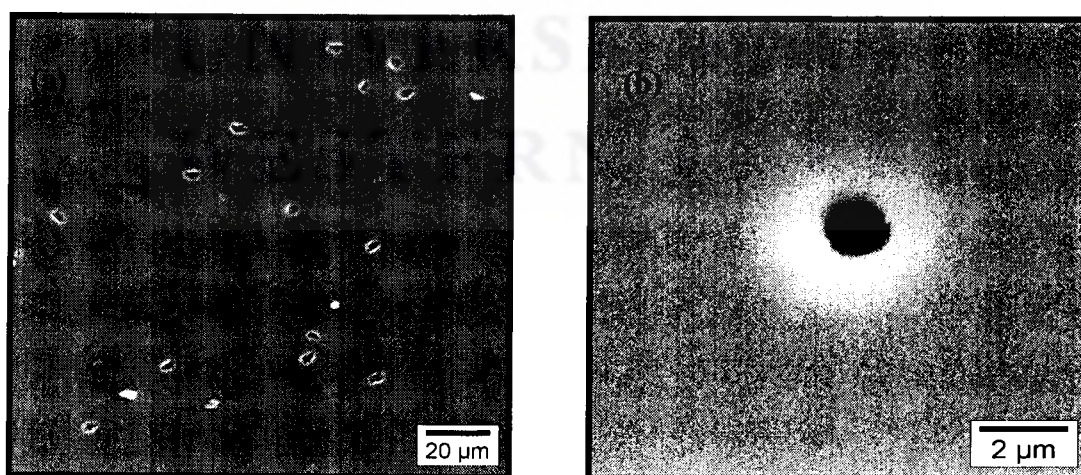
Figure 3.10   Scanning electron micrograph of sample B annealed at 450 °C with magnifications of (a) $\times$ 0.8 k and (b) $\times$ 1.3 k.

3.5 CONCLUSION

In this chapter we have examined the effects of isochronal annealing on H bonding and migration in HW-deposited a-Si:H samples with different H-concentrations and bonding configurations, using IR absorption spectra. The study clearly shows that the annealing behaviour is in fact determined by the as-deposited H concentration and bonding configuration, which eventually determines the stability of the material. This observation is consistent with similar studies performed on plasma-deposited a-Si:H and H_2^+-implanted a-Si.

Sample A, with low H-concentration and superior microstructure ($R^* \ll 0.1$), remains homogeneous at relatively high temperatures up to 400 °C. However, H-diffusion occurs at temperatures below the growth temperature, due to an increase in the network disorder (to be discussed in the next chapter). The site of H emission under thermal annealing has been identified as the isolated $\equiv$Si–H bond, resulting in a reduction in the $\equiv$Si–H bond strength.

Sample B, with high H-concentration and inferior microstructure ($R^* > 0.5$), proves to be unstable at relatively low temperatures. The IR absorption spectra show that changes in the microstructure occur at temperatures below 200 °C. H-diffusion occurs and temperatures > 300 °C, where H is removed preferentially from $\equiv$Si–H bonds on void surfaces. Therefore, the site of H emission under thermal annealing for sample B has been identified as the $\equiv$Si–H bond in both the isolated and clustered (on void surfaces) phases, thereby reducing the strength of both bonding configurations. Furthermore, H out-diffusion occurs via an accumulation of H_2 molecules in high-pressure bubbles, which eventually opens by explosion and consequently results in the blistering of the sample surface.

In summary, the metastable defect site under thermal annealing in HW-deposited a-Si:H has been identified as the $\equiv$Si–H bond (isolated and on void surfaces), resulting in H-diffusion and subsequently in the formation of Si dangling bonds

and weak $\equiv$Si–H bonds. This mechanism is in agreement with that of Biswas *et al.* [3.22] and Branz [3.5].

Future experiments to study the mechanism of H-diffusion should include thermal desorption spectroscopy (TDS), secondary ion mass spectroscopy (SIMS) and high-resolution transmission electron microscopy (HR-TEM).

51

REFERENCES

[3.1]   D. L. Staebler and C. R. Wronski, Appl. Phys. Lett. **31** (1977) 292

[3.2]   I. Hirabayashi, K. Morigaki and S. Nitta, Jpn. J. Appl. Phys **19** (1980) L357

[3.3]   H. Dersch, J. Stuke and J. Beichler, J. Appl. Phys. **38** (1981) 456

[3.4]   W. B. Jackson, Phys. Rev. **B 41** (1990) 10257

[3.5]   M. Branz, Solid State Comm. **105** (1998) 387

[3.6]   D. Roy, C. Longeaud and O. Saadane, J. Non-Cryst. Solids **299 – 302** (2002) 511

[3.7]   H. Touir, J. F. Morhange and J. Dixmier, Solid State Comm. **110** (1999) 315

[3.8]   S. Sheng, G. Kong and X. Liao, Solid State Comm. **116** (2000) 519

[3.9]   W. Y. Ho and C. Surya, Microelectronics Reliability **41** (2001) 913

[3.10] R. Rüther, J. Livingstone, N. Dytlewski and D. Cohan, Thin Solid Films **271** (1995) 151

[3.11] R. Rüther, J. Livingstone, N. Dytlewski and D. Cohan, J. Appl. Phys. **79 (1)** (1996) 175

[3.12] A. H. Mahan and M. Vanecek, AIP Conf. Proc. **234** (1991) 195

[3.13] C. J. Arendse, in "Hydrogenated Amorphous Silicon: Optical Properties and Hydrogen Concentration", M.Sc. thesis, University of the Western Cape, Bellville, South Africa (1999)

[3.14] G. Lucovsky, R. J. Nemanich and J. C. Knights, Phys. Rev. **B 19** (1970) 2064

[3.15] H. Shanks, C. J. Fang, L. Ley, M. Cardona, F. J. Demond and S. Kalbitzer, Phys. Status Solidi **B 100** (1980) 43

[3.16] M. J. van den Boogaard, in "Microvoids and Hydrogen Diffusion in Hydrogenated Amorphous Silicon", Ph.D. thesis, Utrecht University, Utrecht, The Netherlands (1992)

[3.17] R. A. Street, Physica **B 170** (1991) 69

[3.18] A. H. Mahan, L. M. Gedvilas and J. D. Webb, J. Appl. Phys. **87 (4)** (2000) 1650

[3.19] W. B. Jackson and C. C. Tsai, Phys. Rev. **B 45** (1992) 6564

[3.20] G. Lucovsky, Z. Zing, Z. Lu, D. R. Lee and J. L. Whitten, J. Non-Cryst. Solids **182** (1995) 90

[3.21] S. Acco, in "Structural Defects and Hydrogen Clustering in Amorphous Silicon", Ph.D. thesis, Utrecht University, Utrecht, The Netherlands (1997)

[3.22] R. Biswas and B. C. Pan, Appl. Phys. Lett. **72** (1998) 371

[3.23] R. Biswas, Qiming Li, B. C. Pan and Y Yoon, Phys. Rev. **B 57** (1998) 2253

[3.24] C. Godet, Philos. Mag. **B 77** (1998) 765

[3.25] M. H. Branz, Phys. Rev. **B 59** (1999) 5498

[3.26] X. Zou, Y. C. Chan, D. P. Webb, Y. W. Lam, Y. F. Hu, C. D. Beling, S. Fung and H. M. Weng, Phys. Rev Lett. **84** (2000) 769

[3.27] R. Rüther and J. Livingstone, Thin Solid Films **251** (1994) 30

53

CHAPTER 4

Structural Order and

Optical Band Gap

4.1 INTRODUCTION

It is generally accepted that hydrogen incorporation in amorphous silicon not only reduces the density of mid gap states, but also provides more structural flexibility to the amorphous network [4.1], which is evident by the narrowing of the valence and conduction band tail states upon hydrogenation [4.2]. Furthermore, it has been shown that both the hydrogen concentration and the structural order in a-Si:H are both critical factors which eventually determines the stability of the material under light illumination [4.3].

Raman scattering has been employed to provide information on the structural changes in the amorphous network, of which the average bond-angle variation is the key parameter, mainly because of its extreme sensitivity to changes in the small range order. In this chapter we report on the effect of isochronal annealing on the structural order and optical band gap of HW-deposited a-Si:H with different H-concentrations.

Our attention will be specifically focussed on the relation between H-diffusion and changes in the structural disorder, as discussed in the previous chapter. In addition to this we will investigate the influence of the average bond-angle variation and the H-concentration on the optical band gap and possibly provide a correlation between these properties.

This chapter is divided primarily into two main sections; i.e. the effect of isochronal annealing on the structural order (section 4.3) and optical band gap (section 4.4). In each section the quantitative data analysis procedures of the characterisation techniques are discussed, followed by the results and discussion. Firstly, in the next section, the experimental details of the sample preparation, heat treatments and characterisation techniques are described. Finally, in section 4.5 concluding remarks are drawn.

4.2 EXPERIMENTAL DETAILS

The samples under investigation in this chapter; i.e. samples A and B, is the same samples discussed in section 3.2.1 and the heat treatment procedures are identical to that discussed in section 3.2.2.

Raman scattering spectra were collected in the region $0 - 1000$ cm^{-1} in backscattering geometry, using the 514.5 nm line of a Spectra Physics Ar^{+}-ion laser detector (Debye Institute, Utrecht University). A Spex triple-grating monochromator was used to disperse the scattered light onto a liquid-nitrogen cooled EG&G CCD detector. The frequency shifts were calibrated using Rubidium emission lines. A detailed description of the Raman scattering set-up is described elsewhere [4.4]. Raman measurements were performed on samples deposited on Corning 7059 substrates to allow for the detection of the 520 cm^{-1} crystalline peak of the a-Si:H sample without any crystalline contributions from the substrate. The ambient temperature in the Raman set-up amounted to 21 °C.

Optical reflection and transmission measurements were performed on samples deposited on Corning 7059 substrates in the energy range 1.2 – 2.4 eV, with an energy resolution of 3 meV (Debye Institute, Utrecht University). These measurements were used to calculate the film thickness, refractive index and absorption coefficient. The optical band gap was calculated using the Tauc-convention, assuming parabolic band tails [4.5].

4.3 STRUCTURAL ORDER

4.3.1 DATA ANALYSIS: RAMAN SCATTERING

For quantitative analysis, the Raman scattering spectra were deconvoluted into either four or five Gaussians. They are the a-Si transverse-optic (TO) mode centred at 480 cm^{-1}, the longitudinal-optic (LO) mode centred at $\sim$ 445 cm^{-1}, the longitudinal-acoustic (LA) mode centred at $\sim$ 330 cm^{-1}, a hydrogen-related mode at 620 cm^{-1} and, depending on the presence of the crystallinity, the c-Si TO mode centred at $\sim$ 520 cm^{-1}. Figure 4.1 shows an example of a Raman spectrum of an a-Si:H sample with no detectable crystalline phase. There exists a linear relation between the half-width-half-maximum (HWHM) of the a-Si TO-peak, $\Gamma/2$, and the average bond-angle variation [4.6], $\Delta\vartheta_b$, i.e.:

$$\Gamma/2 = 7.4 + 3.2\Delta\vartheta_b \qquad (4.1)$$

where Γ and $\Delta\vartheta_b$ are measured in cm^{-1} and degrees, respectively. Γ is determined at the high energy side of the TO-peak.

For a-Si:H, maximally ordered and maximally disordered networks have values of 7.0° – 8.2° and 11.0° – 14.1° for $\Delta\vartheta_b$, respectively [4.7].

The crystalline fraction, c_f, is defined as [4.8]:

$$c_f = \frac{I_{520}}{I_{520} + 0.1\exp(-x/250)I_{480}} \qquad (4.2)$$

where I_{480} and I_{520} are the deconvoluted intensity of the a-Si and c-Si TO-peaks, respectively.
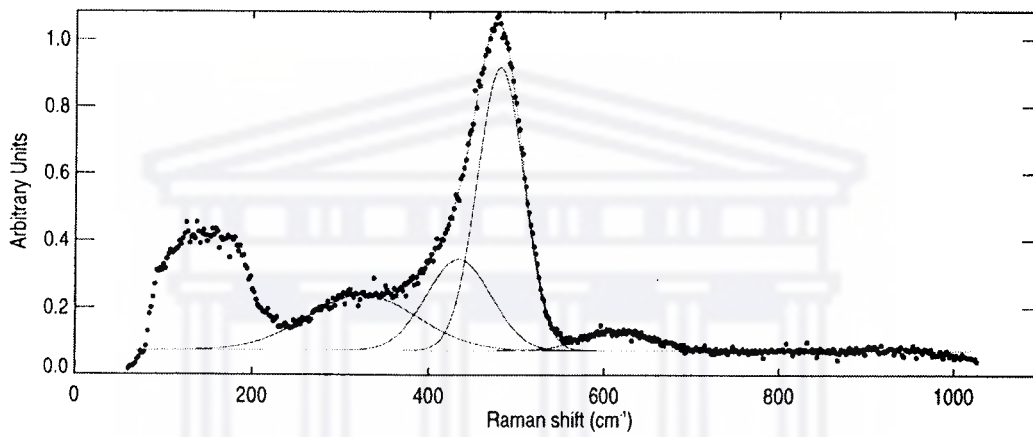
Figure 4.1 Example of a deconvoluted Raman spectrum of an a-Si:H sample with no detectable crystalline contribution.

4.3.2 THERMALLY INDUCED PHASE TRANSITIONS

The Raman spectra of samples A and B in the as-deposited and final annealing states are shown in Figures 4.2 and 4.3, respectively. The spectra were normalized to the height of the a-Si TO-peak. No emerging c-Si TO-peaks are observed at ~ 520 cm^{-1} before and after annealing, illustrating that no amorphous-to-crystalline phase transitions occur in both samples as annealing progresses. Further annealing of both samples up to 550 °C induces no detectable phase transitions (not shown). This is consistent with the observations of Spinella *et al.* [4.9] who have shown that crystal grain nucleation in a-Si occurs at temperatures above 560 °C.
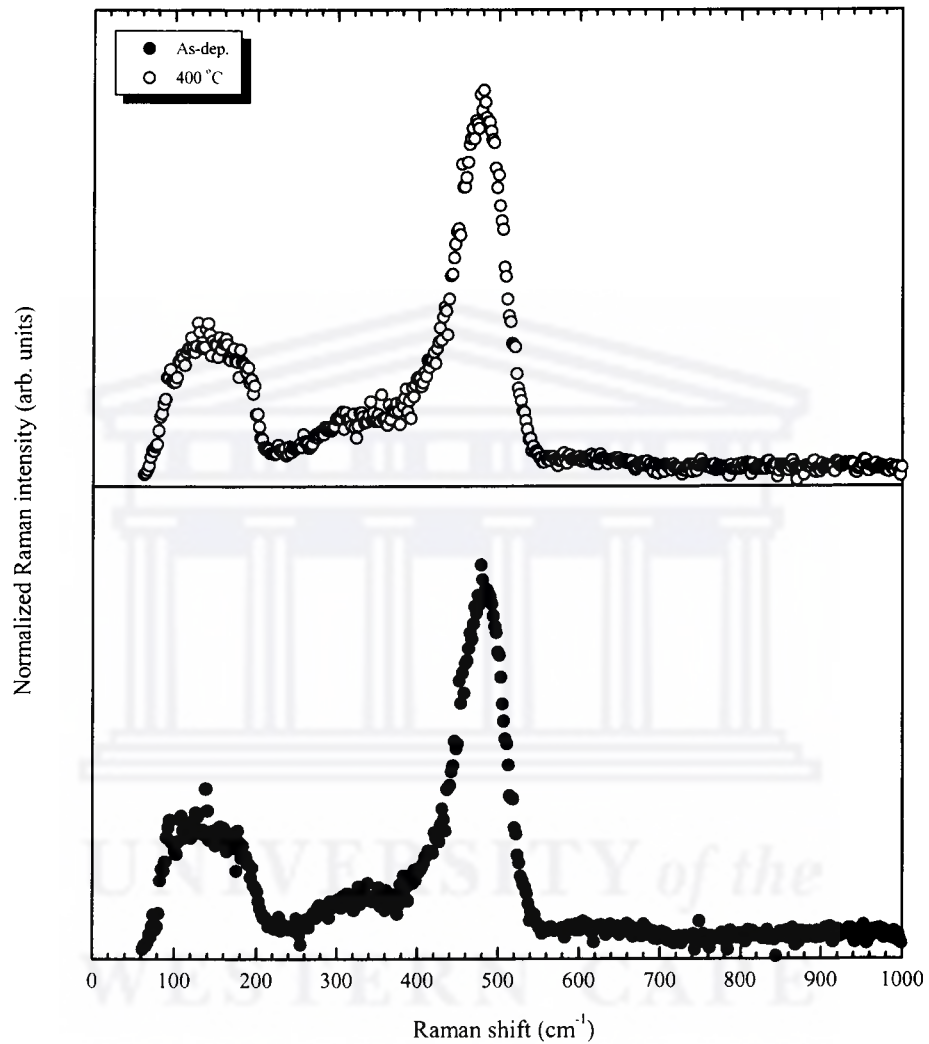
Figure 4.2   Stacked Raman spectra of sample A in the as-deposited state (solid circles) and after annealing at 400 °C (open circles).
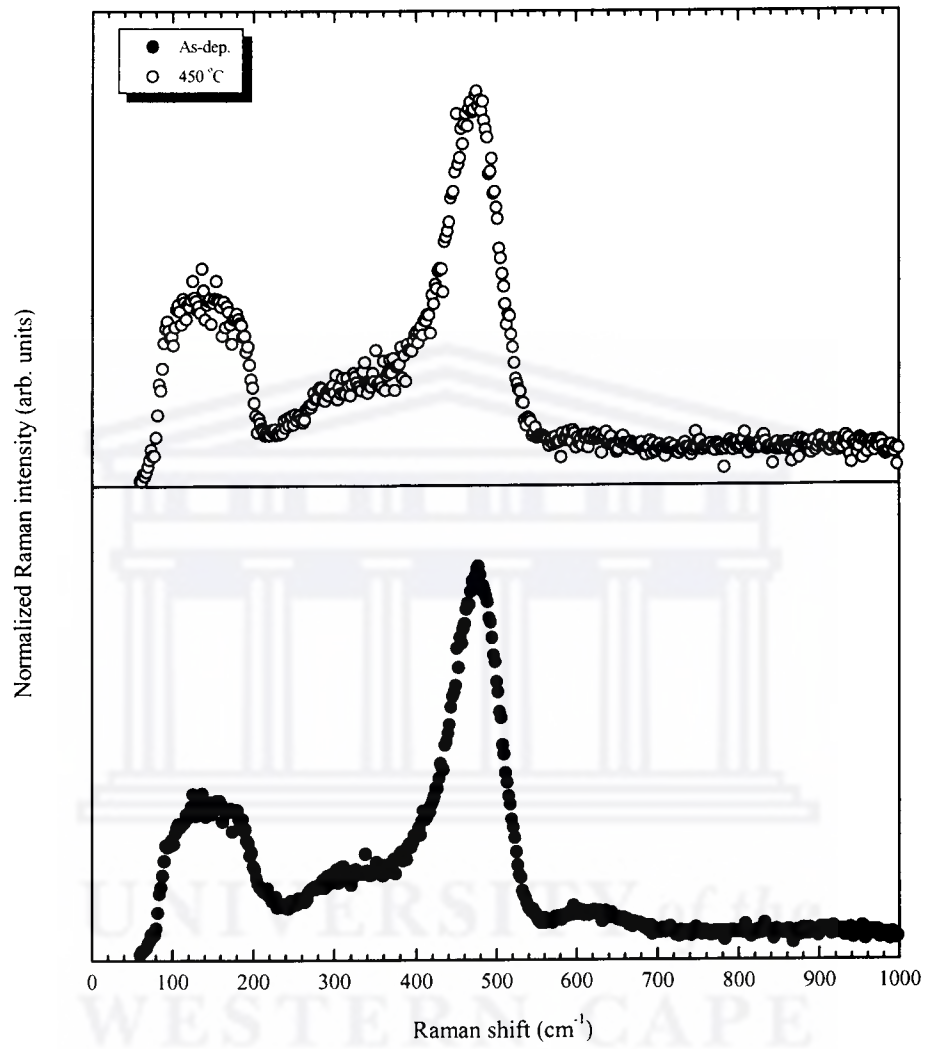
Figure 4.3   Stacked Raman spectra of sample B in the as-deposited state (solid

circles) and after annealing at 450 °C (open circles).

4.3.3 EFFECTS OF ANNEALING

In the as-deposited state the $\Gamma/2$-value for sample A amounts to 30.69 cm^{-1}, corresponding to a $\Delta\vartheta_b$-value of 7.28°. For sample B the $\Gamma/2$-value in the as-deposited state amounts to 33.12 cm^{-1}, corresponding to a $\Delta\vartheta_b$-value of 8.03°. The $\Gamma/2$-value of sample A is among the lowest determined for device-quality HW a-Si:H [4.7, 4.10], illustrating the superior structural quality of this sample.
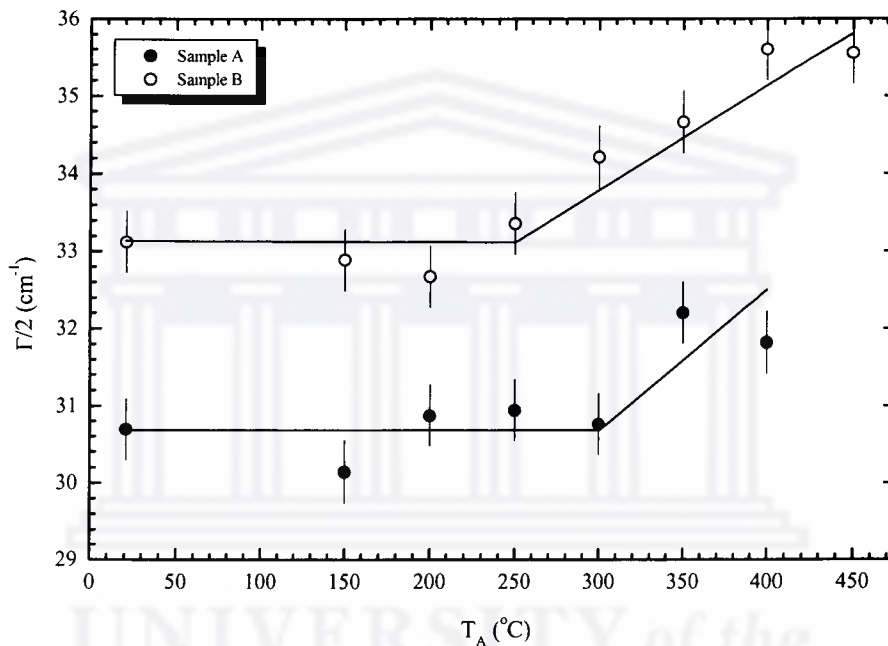
Figure 4.4 $\Gamma/2$ as a function of annealing temperature for sample A (solid circles) and sample B (open circles). The lines are drawn to guide the eye.

The plot of $\Gamma/2$ as a function of annealing temperature for samples A and B is shown in Figure 4.4. Annealing sample A at temperatures up to 300 °C induces no considerable change in $\Gamma/2$. For $T_A \geq 350$ °C a slight increase, of ~ 1 cm^{-1}, in $\Gamma/2$ is observed. A significant linear increase in $\Gamma/2$ is observed for sample B at $T_A \geq 300$ °C. These observations are consistent with studies performed on maximally ordered plasma-deposited a-Si:H with H-concentrations in excess of 10 at.% [4.11], indicating that our samples are maximally ordered. Similar studies

60

performed on irradiated a-Si and more disordered a-Si:H show a distinct decrease in $\Gamma/2$ with increasing annealing temperature, which is attributed to structural relaxation [4.7, 4.12 – 4.14].

The increase in $\Gamma/2$ is associated with an increase in the network disorder, which is the cause of hydrogen being incorporated into disorder-induced shallow states, which consequently results in H-diffusion. Figure 4.5 shows the plot of the concentration of bonded hydrogen, determined from IR absorption spectra, as a function of $\Gamma/2$. Figure 4.6 shows the plot of the displacement of the 2000 cm^{-1}-peak position as a function of $\Gamma/2$. An inverse linear relationship between C_H and $\Gamma/2$ is evident, which supports and proves our earlier speculation that H-diffusion is caused primarily by an increase in the network disorder.
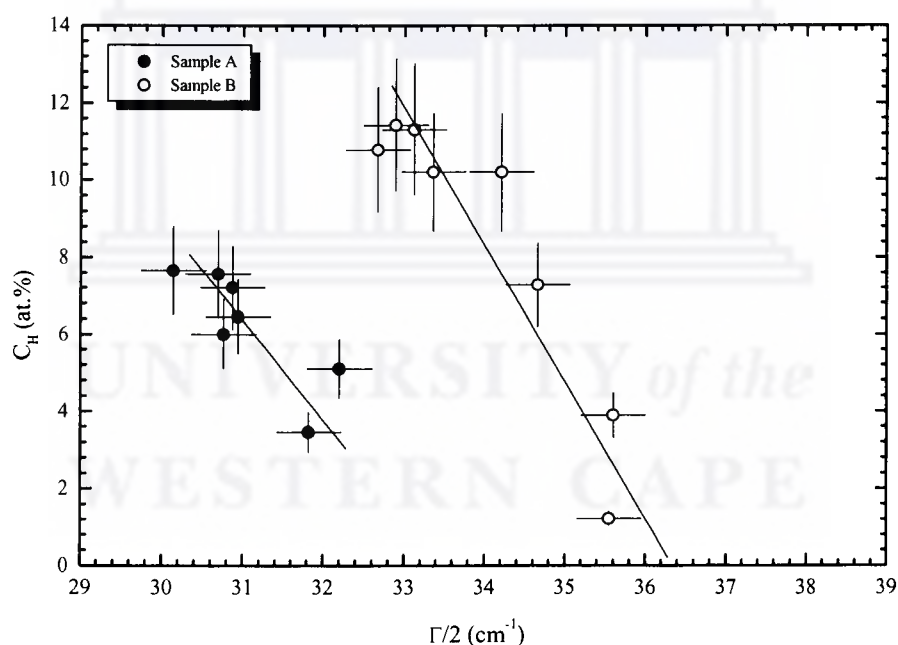
Figure 4.5   Hydrogen concentration as a function of $\Gamma/2$ for sample A (solid circles) and sample B (open circles). The lines are linear fits through the data.
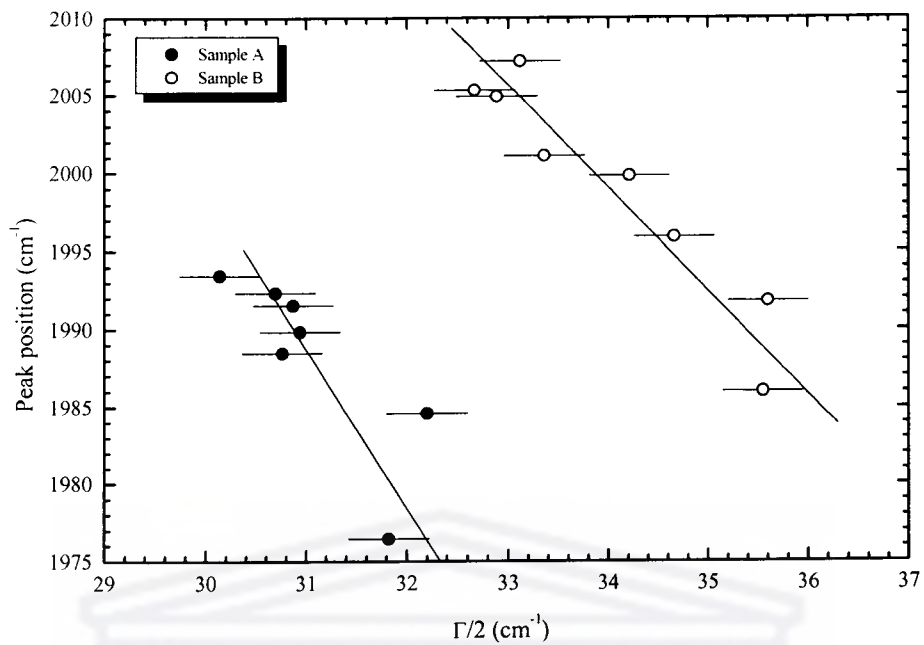
Figure 4.6 Displacement of the 2000 cm^{-1}-peak position as a function of $\Gamma/2$ for sample A (solid circles) and sample B (open circles). The lines are linear fits through the data.
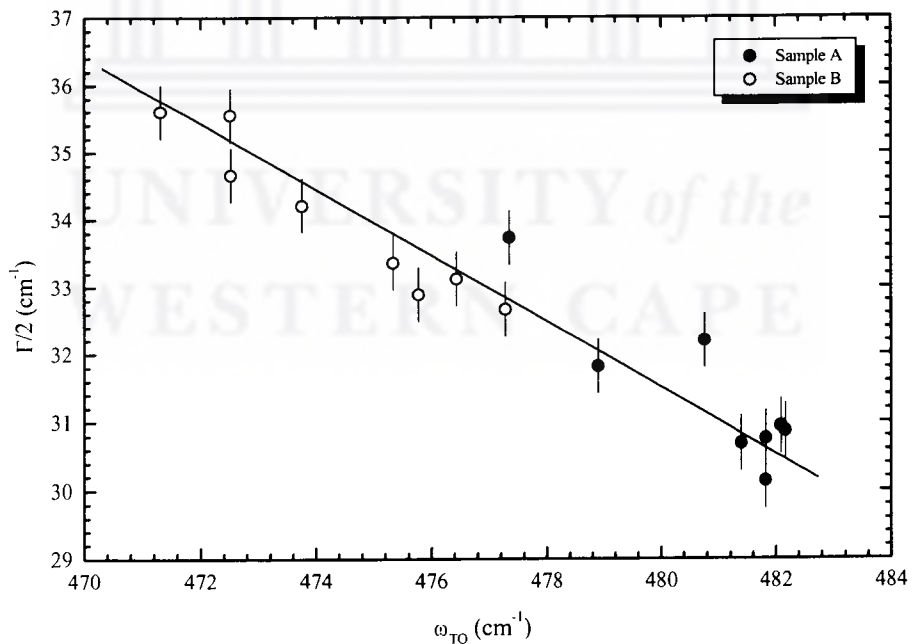
Figure 4.7 $\Gamma/2$ as a function of the peak position of the a-Si TO-peak for sample A (solid circles) and sample B (open circles). The line is a linear fit through the data.

62

Previous research has shown that the position of the a-Si TO-peak, ω_{TO}, can be related to structural changes in the amorphous network [4.14]. In Figure 4.7 we plot $\Gamma/2$ as a function of ω_{TO}, which shows an inverse linear dependence. Thus a shift of ω_{TO} to higher wave numbers is characteristic of structural relaxation of the amorphous network.

4.4 OPTICAL BAND GAP

4.4.1 DATA ANALYSIS

The data analysis of the optical reflection and transmission measurements was discussed in section 2.4 and is described in detail elsewhere [4.15]. The optical band gap was calculated from the absorption coefficient and the refractive index, using the Tauc-convention [4.5]. In Figure 4.8 we show the plots of $[\alpha(E)n(E)E]^{1/2}$ versus E in the as-deposited state for samples A and B. The optical band gap, E_{Tauc}, was determined by extrapolating $[\alpha(E)n(E)E]^{1/2}$ to $\alpha(E) = 0$, for $\alpha(E) \geq 10^3$ cm^{-1}.
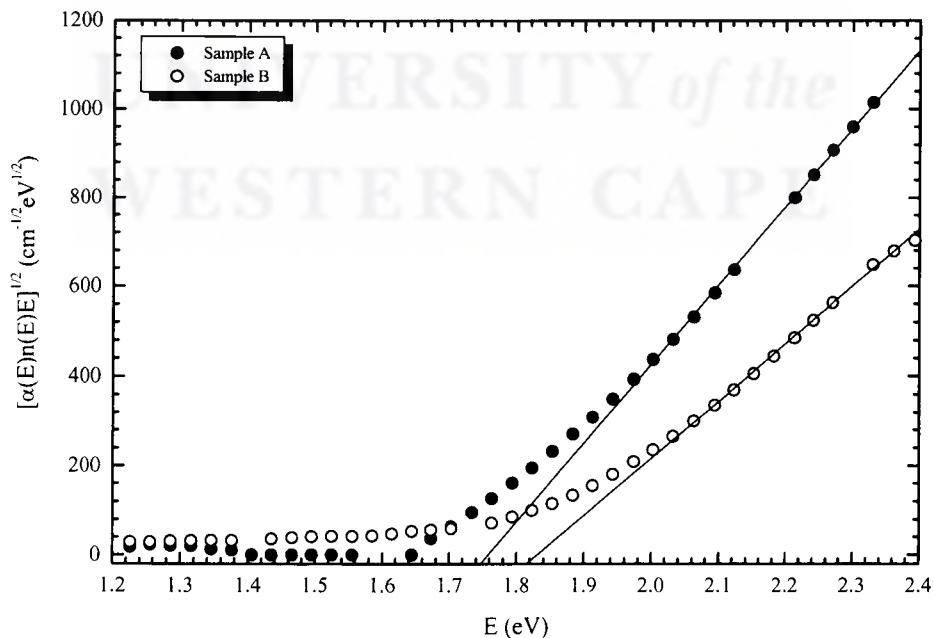
Figure 4.8   Plots of $[\alpha(E)n(E)E]^{1/2}$ versus E in the as-deposited state for sample A (solid circles) and sample B (open circles).

The optical band gap of sample A amounts to 1.758 ± 0.004 eV, characteristic of device-quality HW-deposited a-Si:H with C_H ~ 8 at.%. The optical band gap for sample B amounts to 1.817 ± 0.005 eV, which is typical of poor-quality HW-deposited a-Si:H with H-concentrations in excess of 10 at.% [4.16 – 4.17].

4.4.2 EFFECTS OF ANNEALING: HYDROGEN VS. DISORDER

The optical band gap of a-Si:H is one of the most widely studied subjects in solar cell applications, since it is related to the electronic structure of the material and, more importantly, since the efficiency of solar cells made from this material is directly related to it. It is generally accepted that the band gap is dependent on both the H-concentration and the structural order [4.2, 4.7, 4.15 – 4.21].

The optical band gap as a function of annealing temperature for samples A and B is shown in Figure 4.9. Annealing samples A and B at $T_A \leq 300$ °C and $T_A \leq 250$ °C, respectively, induces no change in E_{Tauc}. After annealing sample A at 350 °C a linear decrease in E_{Tauc} is observed. Annealing sample B at temperatures ranging between 300 – 350 °C produces a linear decrease in E_{Tauc}, after which E_{Tauc} reaches a saturation level at $T_A > 350$ °C. It should be noted that similar trends in the cubic band gap for samples A and B were observed, using the method proposed by Klazes *et al.* [4.22] (not shown).

Müller *et al.* [4.23] have shown that the slope of the linear fit through the data in Figure 4.7, B_{Tauc}, is proportional to the density of states in the valence and conduction band tails. In Figure 4.10 we plot B_{Tauc} as a function of annealing temperature for samples A and B.
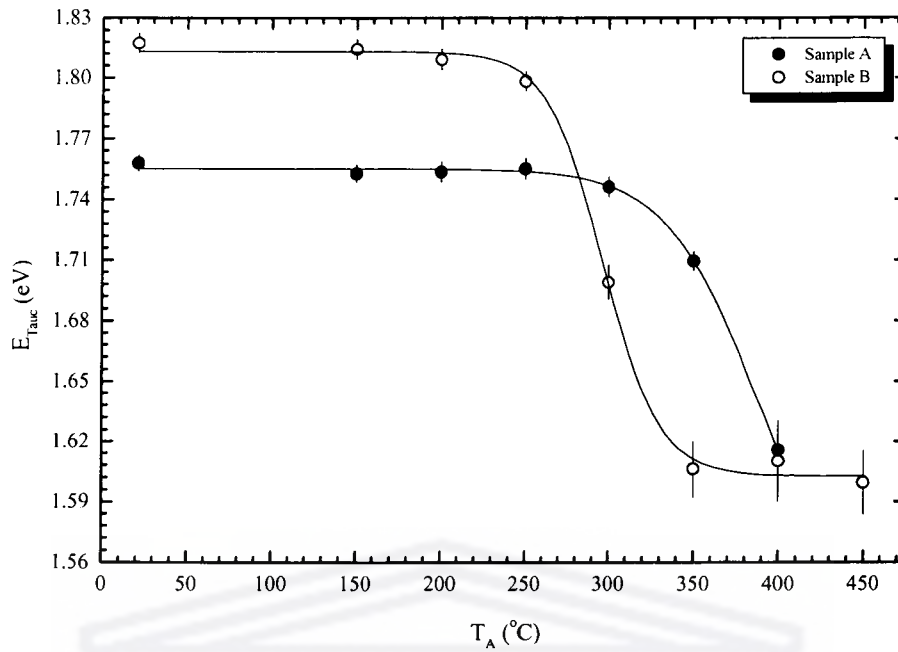
Figure 4.9 The optical band gap, determined from a $[\alpha(E)n(E)E]^{1/2}$-fit, as a function of annealing temperature for sample A (solid circles) and sample B (open circles). The lines are drawn to guide the eye.
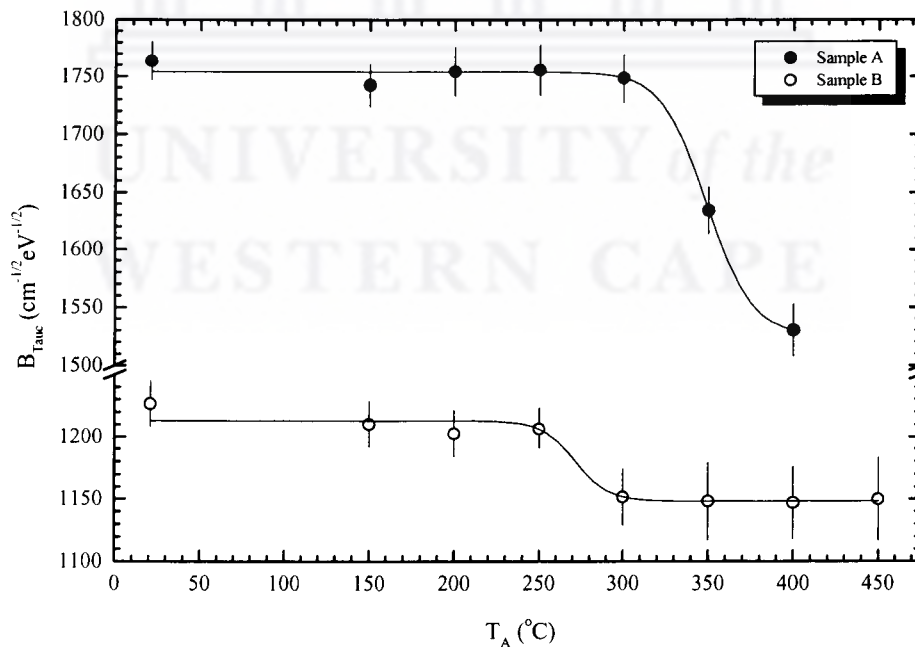
Figure 4.10 The slope of the linear fit through $[\alpha(E)n(E)E]^{1/2}$, as a function of annealing temperature for sample A (solid circles) and sample B (open circles). The lines are drawn to guide the eye.

65

Similar trends in E_{Tauc} and B_{Tauc} are observed with increasing annealing temperature. Therefore we conclude that the decrease in B_{Tauc} is associated with the broadening of the valence and conduction band tails, thereby pinning the valence and conduction band edges closer together resulting in a reduction in E_{Tauc}. The broadening of the valence and conduction bands is caused by an increase in the structural disorder, as seen by the increase in $\Gamma/2$ in Figure 4.4. The increase in $\Gamma/2$ is also the primary cause of H-diffusion, as discussed in Figure 4.5, which results in the creation of Si dangling bonds, thereby causing a reduction in E_{Tauc}.

To summarise, changes in E_{Tauc} is fully attributed to changes in the network disorder, which can be divided into two contributions. The first being the broadening of the conduction and valence band tails, while the second is the creation of Si dangling bonds caused by H-diffusion.

4.5 CONCLUSION

In this chapter the effect of isochronal annealing on the structural order and optical band gap of two HW-deposited a-Si:H samples, with different H-concentrations, has been investigated. Raman scattering was used to quantify the degree of disorder in the amorphous network, which was related to H-diffusion and the optical band gap.

Our results suggest that both samples remain purely amorphous at temperatures as high as 550 °C. The stability of the structural order is dependent on the initial H-concentration; i.e. a-Si:H with a low H-concentration remain stable at relatively higher temperatures compared to that of a-Si:H with high H-concentrations. This is evident by the slight increase of ~ 1 cm^{-1} in $\Gamma/2$ for sample A at 400 °C as compared to a 3 cm^{-1} increase in $\Gamma/2$ for sample B at the same temperature.

We have successfully shown that H-diffusion is primarily caused by an increase in the network disorder, resulting in the creation of Si dangling bonds. In addition to

this an increase in the network disorder also causes a broadening of the valence and conduction band tails. Both of the above-mentioned observations result in a reduction in the optical band gap.

REFERENCES

[4.1]   R. A. Street, in "Hydrogenated Amorphous Silicon", Cambridge University Press, Cambridge (1991)

[4.2]   L. Ley, in "The Physics of Hydrogenated Amorphous Silicon II", edited by J. D. Joannopoulos and G. Lucovsky, Springer-Verlag, Berlin (1984)

[4.3]   R. A. Street and K. Winer, Phys. Rev. **B 40** (1989) 6236

[4.4]   A. M. Brockhoff, in "Hydrogen-Related Modifications of Amorphous Silicon and Silicon Nitride", Ph.D. thesis, Utrecht University, Utrecht, The Netherlands (2001)

[4.5]   J. Tauc, in "Optical Properties of Solids", ed. F. Abeles, North-Holland Publ., Amsterdam (1972)

[4.6]   D. Beeman, R. Tsu and M. F. Thorpe, Phys. Rev. **B 32** (1985) 874

[4.7]   A. J. M. Berntsen, in "Structural Disorder in Pure and Hydrogenated Amorphous Silicon", Ph.D. thesis, Utrecht University, Utrecht, The Netherlands (1993)

[4.8]   E. Bustarret, M. A. Hachinia and M. Brunel, Appl. Phys. Lett. **52** (1988) 1675

[4.9]   C. Spinella, S. Lombardo and F. Priolo, J. Appl. Phys. **84** (1998) 5383

[4.10] A. H. Mahan, D. L. Williamson and T. E. Furtak, in "Amorphous and Microcrystalline Silicon Technology" (1997), edited by S. Wagner, M. Hack, E. A. Schiff, R. E. I. Schropp and I. Shimizu (Materials Research Society, Pittsburgh (1997), Vol. 467, pp. 657 – 662

[4.11] S. Acco, in "Structural Defects and Hydrogen Clustering in Amorphous Silicon", Ph.D. thesis, Utrecht University, Utrecht, The Netherlands (1997)

[4.12] H. Touir, J. F. Morhange and J. Dixmier, Solid State Commun. **110** (1999) 315

[4.13] O. Gamulin, M. Ivanda, U. V. Desnica and K. Furić, J. Non-Cryst. Solids **227 – 230** (1998) 943

[4.14] W. C. Sinke, T. Warabisako, M. Miyao, T. Tokuyama, S. Roorda and F. W. Saris, J. Non-Cryst. Solids **99** (1988) 308

[4.15]   M. J. van den Boogaard, in "Microvoids and Hydrogen Diffusion in Hydrogenated Amorphous Silicon", Ph.D. thesis, Utrecht University, Utrecht, The Netherlands (1992)

[4.16]   K. F. Feenstra, in "Hot-wire Chemical Vapour Deposition of Amorphous Silicon and the Applications in Solar Cells", Ph.D. thesis, Utrecht University, Utrecht, The Netherlands (1998)

[4.17]   K. F. Feenstra, R. E. I. Schropp and W. F. van der Weg, J. Appl. Phys. **85 (9)** (1999) 6843

[4.18]   K. H. M. Maessen, M. J. M. Pruppers, J. Bezemer, F. H. P. M. Habraken and W. F. van der Weg, Mater. Res. Soc. Symp. Proc. **95** (1987) 201

[4.19]   H. Meiling, M. J. van den Boogaard, R. E. I. Schropp, J. Bezemer and W. F. van der Weg, Mater. Res. Soc. Symp. Proc. **192** (1990) 645

[4.20]   H. Meiling, in "Deposition of Amorphous Silicon Thin Films and Solar Cells", Ph.D. thesis, Utrecht University, Utrecht, The Netherlands (1991)

[4.21]   N. Maley and J. S. Lannin, Phys. Rev. **B 36** (1987) 1146

[4.22]   R. H. Klazes, M. H. L. M. van den Broek, J. Bezemer and S. Radelaar, Phil. Mag. **B 45** (1982) 377

[4.23]   G. Müller, H. Mannsperger and S. Kalbitzer, Phil. Mag. **B 53** (1986) 257

CHAPTER 5

Structural Characterisation:

Positron Annihilation

5.1 INTRODUCTION

Positron annihilation spectroscopy is a set of techniques based on the ability of positrons when these meet open-volume imperfections (defects) in a solid, to become localized and eventually annihilated by nearby electrons [5.1]. Its sensitivity covers a wide range of defect types and concentrations and is increasingly being used as a sensitive probe to characterise low concentrations of open-volume defect sites [5.2 – 5.3]. Included in these set of techniques are positron lifetime and Doppler-broadening spectroscopies.

The positron lifetime is dependent on the local electron density around the defect site. The defect-related lifetime, which is inversely proportional to the annihilation probability, increases as the electron density around the defect site decreases with increasing size. Therefore, positron lifetime spectroscopy is most sensitive to the defect size and concentration. Doppler-broadening spectroscopy is a form of electron-momentum spectroscopy that measures the momentum imparted to the annihilation quanta by the participating electron. The momentum imparted is measured by an energy shift due to the centre-of-mass motion of the positron-electron annihilation pair. This information is contained in the energy broadening

of the 511 keV γ-ray peak. Specific line-shape parameters can be used to quantify the fraction of positrons annihilating with different electron distributions. The low-electron-momentum (valence) fraction, generally referred to as the S-parameter, depends primarily on the size and concentration of the open-volume defect. An increase in the S-parameter is associated with an increase in the defect size, concentration or both. On the other hand, the high-electron-momentum (core) fraction, generally referred to as the W-parameter, is sensitive to the electronic structure at the annihilation site. For a specific spectrometer, the S- and W-parameters now uniquely define the electronic configuration around a specific defect. Used as complementary methods, positron lifetime and Doppler-broadening spectroscopies can provide useful information about the size, concentration and type of defects present in a solid.

Positron annihilation spectroscopy has a long history in the detection of defect structures in solid-state applications and is well established in the study of crystalline semiconductors [5.1, 5.4]. A variety of positron techniques have been applied to the study of a-Si and a-Si:H produced by different techniques [5.5 – 5.15]. It has been shown that for unhydrogenated a-Si the dominant traps for positrons are microvoids, present in large concentrations [5.5 – 5.6]. Plasma-deposited a-Si:H appears to have a lower, but still significant microvoid concentration, which is attributed to the high concentration of hydrogen bonded in the clustered phase [5.5, 5.7 – 5.9]. Recently several HW-deposited a-Si:H samples, deposited by our group, have been characterised by lifetime and Doppler-broadening spectroscopies [5.10 – 5.13]. The dominant defect in HW-deposited a-Si:H has been identified as the decorated dangling bond complex, which has similar annihilation characteristics as the monovacancy in crystalline silicon [5.9 – 5.11].

In this chapter we investigate the effect of isochronal annealing on the defect structure of HW-deposited a-Si:H using Doppler-broadening spectroscopy, and relate these changes to the changes in the H-concentration and structural order.

This chapter is organised as follows. In the next section the experimental details of the sample preparation, heat treatments and characterisation techniques are described. In section 5.3 the quantitative data analysis of Doppler-broadening spectroscopy will be discussed. The changes in the defect structure will be discussed in section 5.4, followed by concluding remarks drawn in Section 5.5.

5.2 EXPERIMENTAL DETAILS

5.2.1 SAMPLE PREPARATION

Samples A and B have been deposited in the MVSYSTEM deposition chamber at the exact deposition conditions described in section 3.2.1, with the exception of the deposition time to allow for a film thickness of > 800 nm, enabling a clear differentiation between the surface and a-Si:H layer signals in the Doppler-broadening defect-depth profile. The samples were deposited only on Corning 7059 substrates since it has a significantly different electronic configuration than the a-Si:H layer, thus producing well-separated layer and substrate signals [5.10].

5.2.2 HEAT TREATMENTS

Isochronal annealing of sample A was performed in situ in the positron annihilation set-up [5.16] in a vacuum of base pressure 2×10^{-6} Pa (Department of Physics, University of Cape Town). The annealing temperature ranged from 150 – 400 °C, in 50 °C increments. After the annealing temperature was reached the sample was maintained at the particular temperature for 30 minutes, after which the sample was cooled to ambient temperature, followed by the measurements.

5.2.3 CHARACTERISATION

Doppler-broadening electron-momentum spectroscopy was performed using the continuous positron beam at the University of Cape Town [5.16] in a vacuum of base pressure 2×10^{-6} Pa. The incident positron energy was varied from 0.2 – 16.3 keV, which corresponds to a maximum mean implantation depth of ~ 1500 nm in crystalline silicon. At energies ranging between 0.2 – 6.8 keV the energy resolution amounted to 0.3 keV, whereas at energies ranging between 6.8 – 16.3 keV the energy resolution amounted to 0.6 keV. Six measurement runs were performed at all energies with a total collection time of 300 seconds for each run. The ambient temperature at the sample position amounted to 68 ± 2 °C and 79 ± 1 °C for samples A and B respectively.

5.3 DATA ANALYSIS: DOPPLER-BROADENING SPECTROSCOPY

The mean penetration depth of the positrons is dependent on the incident positron energy E and is given by:

$$\bar{z} = \frac{\alpha}{\rho} E^n \qquad (5.1)$$

where α and n are constants; and

ρ is the density of the sample.

Widely accepted empirical values for α and n are 400 $\mu gcm^{-2}keV^{-n}$ and 1.6 respectively [5.17]. As a starting point the density of c-Si [5.18] was used, after which the density was adapted to compensate for difference in the true film thickness determined from optical interferometry and the nominal film thickness

73

determined from the defect-depth profile using equation (5.1). Alternatively the density of the sample can be determined using equation (2.9).

The Doppler-broadening of the 511 keV-peak consists of various components, each associated with a specific positron annihilation process. The S-parameter is defined as the normalized area of the central low-momentum part of the spectrum A_s divided by the area below the whole curve A_o after background subtraction; i.e.

$$S = \frac{A_s}{A_o}$$

(5.2)

where;

$$A_s = \int_{E_o - E_s}^{E_o + E_s} N_D \, dE$$

(5.3)

The W-parameter is defined as the normalized area of the wings A_w divided by the area below the whole curve A_o after background subtraction; i.e.

$$W = \frac{A_w}{A_o}$$

(5.4)

where;

$$A_w = \int_{E_1}^{E_2} N_D \, dE$$

(5.5)

The integration limits are chosen systematically around the energy $E_o = 511$ keV for the calculation of the S-parameter. The integration limits E_1 and E_2 for the W-parameter must be defined in such a way as to have no correlation effects with the S-parameter. After the integration limits E_S, E_1 and E_2 have been identified it was kept fixed for all measurements.

Figure 5.1 shows an example of a Doppler-broadening spectrum of an a-Si:H sample. The spectrum shows the approximate areas used for the calculation of the S- and W-parameters and the energy limits E_1 and E_2.

74
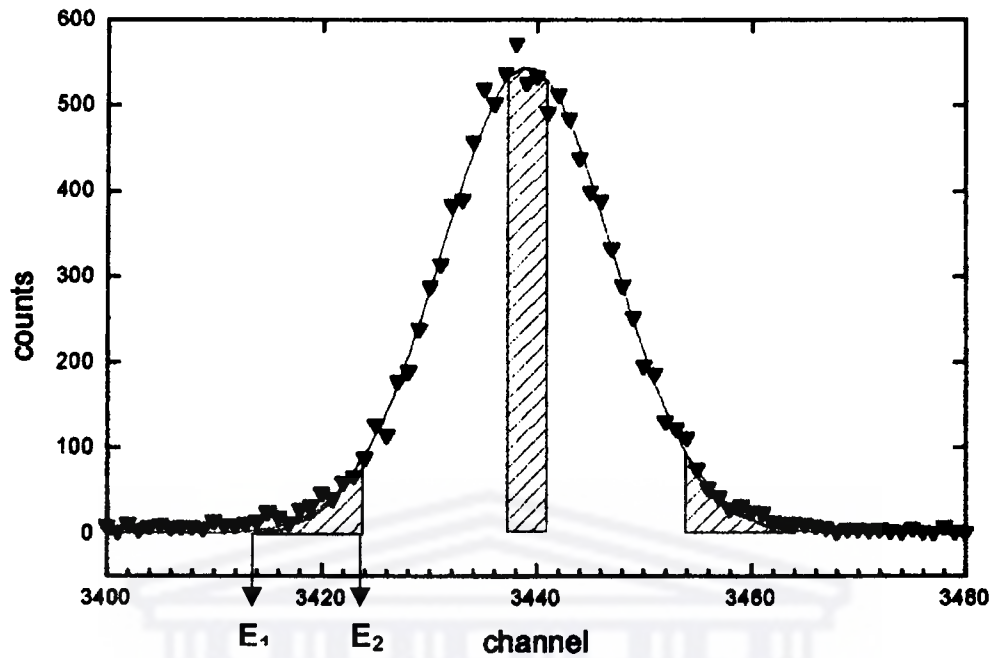
Figure 5.1 Doppler-broadening spectrum (raw data) of an a-Si:H sample. The shaded areas in the center and the wings refer to the approximate areas used for the calculation of the S- and W-parameters, respectively [5.19].

The R-parameter [5.20], which depends only on the defect type and not on the defect concentration, is defined as:

$$R = \left| \frac{S_2 - S_1}{W_2 - W_1} \right| \qquad (5.6)$$

The R-parameter for a particular defect type can be calculated from the graphic presentation of S = S(W) as the slope of the straight line through (W_2, S_2) and (W_1, S_1). The S versus W plots can be used to highlight the presence of different defect types in differently prepared and treated samples.

5.4 RESULTS AND DISCUSSION

5.4.1 AS-DEPOSITED DEFECT-DEPTH PROFILES

The results of the Doppler-broadening analysis for samples A and B in the as-deposited state are shown in Figures 5.2 and 5.3 respectively. It should be noted that the mean nominal depths in these figures were calculated using the density of c-Si. Two different regions can be distinguished, corresponding to the annihilation states of positrons in the a-Si:H layer and at the a-Si:H/substrate interface. For sample A these regions are centred at nominal depths of 180 nm and 800 nm respectively.
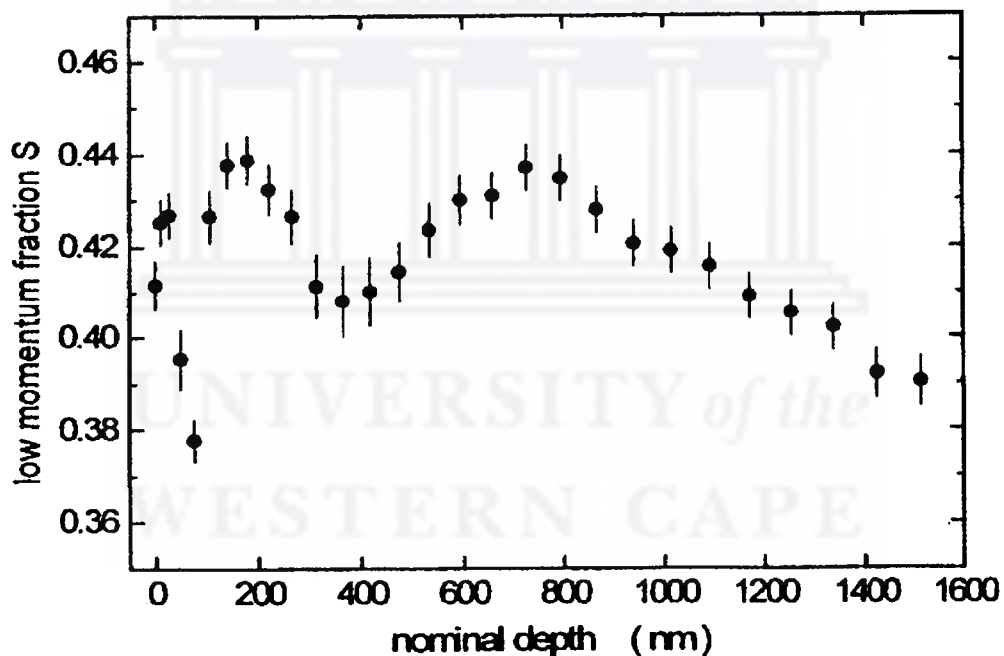
Figure 5.2 Low momentum fraction S as a function of the mean nominal depth, calculated to the mean depth in c-Si, for sample A in the as-deposited state [5.21].

The a-Si:H layer and interface regions for sample B are centred at nominal depths of 110 nm and 730 nm, respectively.
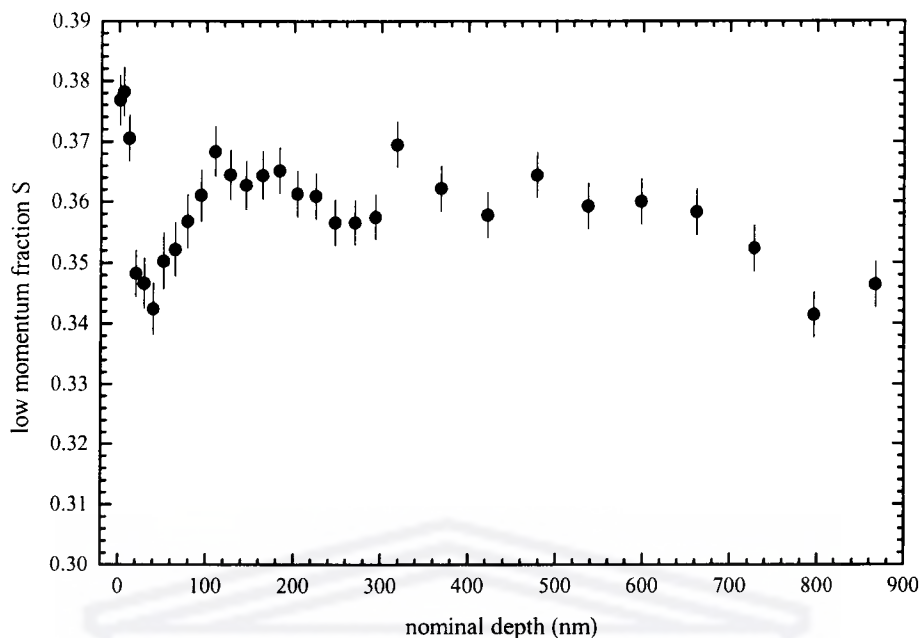
Figure 5.3   Low momentum fraction S as a function of the mean nominal depth, calculated to the mean depth in c-Si, for sample B in the as-deposited state.

Härting *et al.* [5.12] have shown that a relaxation of the amorphous network of HW-deposited a-Si:H results in a higher degree of ordering and consequently in a reduction in the average size of the defects, assuming the same defect type. Therefore, in general, a reduced S-parameter is associated with a higher degree of ordering in the amorphous network. Raman scattering have shown that sample A is more ordered than sample B and therefore we are tempted to predict that the S-parameter of the sample A should be lower than that of sample B. However, this is not seen by the reduced S-parameter of sample B; and consequently it is feasible to assume that the dominant defect type of samples A and B is fundamentally different. However, Figure 5.4 shows that the gradients of the S- vs. W-parameter plots, i.e. the R-parameter, of samples A and B are equal and amounts to ~ 1.038. This illustrates that the samples have the same dominant defect type [5.20], thereby rendering our previous assumption invalid. Britton *et al.* [5.11] have shown that positrons annihilate from a single state, with a lifetime of ~ 330 ps, in sample A. This lifetime is characteristic of the dangling bond complex in a-Si:H [5.1], which is therefore the dominant defect type in samples A and B.

77
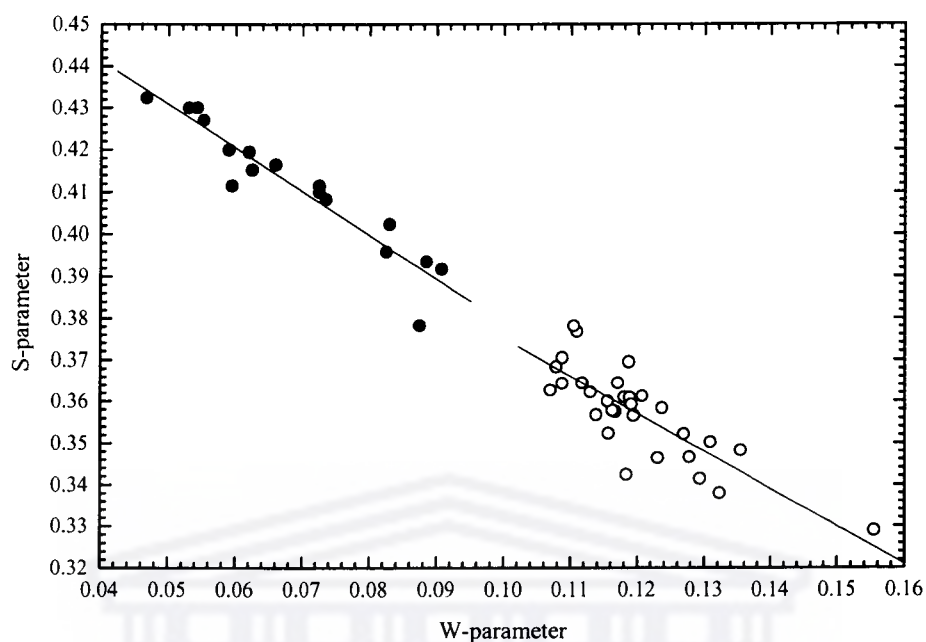
Figure 5.4   S-parameter versus W-parameter in the as-deposited state for
sample A (solid circles) and sample B (open circles). The lines are
linear fits through the data.

The reduced S-parameter of sample B can be explained by the large fraction of
hydrogen bonded in the clustered phase, in particular on the internal surfaces of
microvoids, as shown in the IR spectrum of sample B (Chapter 3). This results in a
reduction of the effective free volume, i.e. defect size, seen by the positron and
consequently results in a reduced S-parameter.

5.4.2 EFFECTS OF ANNEALING

Figure 5.5 shows the plot of the S-parameter as a function of annealing
temperature for sample A [5.11]. The values plotted are an average over an 80 nm-
wide region centred around a mean depth of 180 nm. The errors shown are the
standard deviation of the averaging procedure. The S-parameter increases
monotonically with an increase in temperature up to 350 °C, indicative of an
increase in the defect size, concentration or both.

After annealing the sample at 400 °C a saturation of the S-parameter is observed, implying that the defect structure remains stable.
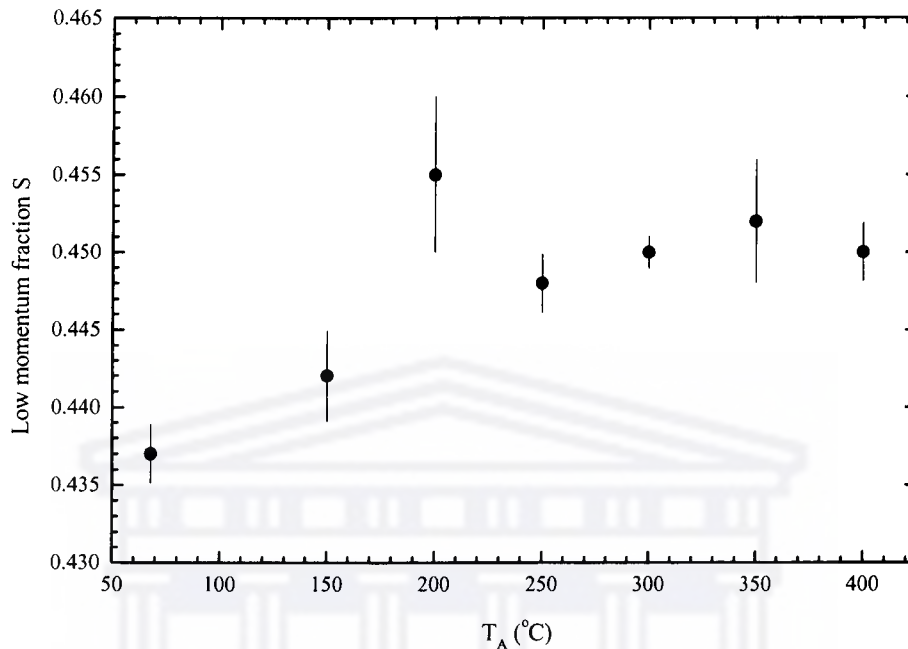
Figure 5.5 Low momentum fraction S as a function of annealing temperature for sample A.

Since no H migration or diffusion is observed at temperatures ≤ 200 °C, the increase in the S-parameter in this temperature range can be attributed to the alignment of native Si dangling bonds, which are already unstable at room temperature [5.1], and can therefore cluster to produce larger open-volume defects or microvoids. At temperatures ≥ 250 °C when H-diffusion occurs the increase in the S-parameter is partly due to the termination of the ≡Si–H bonds, caused by an increased network disorder. This results in the creation of weak ≡Si–H bonds, as seen from the IR absorption spectra, and Si dangling bonds that are indistinguishable from native dangling bonds, thereby increasing number of defects. This is followed by the recombination of two neighbouring H atoms, resulting in the formation of H_2 [5.22] and eventually H-diffusion, assuming H_2 to be the mobile species [5.23]. Zou *et al.* [5.24] suggested this configuration to be

the defect responsible for the Staebler-Wronski effect and is consistent with the infrared results in Chapters 3.

Furthermore, the Si-dangling bonds created as a consequence of H-diffusion are already mobile at room temperature [5.1] and can therefore be unstable and again align to eventually cluster to form larger open-volume defects or microvoids, thereby contributing to an increase in the S-parameter. Positron lifetime spectroscopy confirms that in the as-deposited state there are no microvoids present in sample A. However, the formation of microvoids after annealing sample A at 400 °C becomes evident, as seen by a second void-like lifetime component in the lifetime spectrum that amounts to 691 ± 54 ps [5.11]. Since no clustered phase of hydrogen is observed from the IR absorption spectrum at 400 °C, we can conclude that the internal surfaces of the microvoids are not occupied by hydrogen.

In summary, at temperatures ≤ 200 °C, where no H-diffusion is observed, the native Si dangling bonds cluster to initiate the formation of low concentrations of microvoids. At temperatures ≥ 250 °C, where H-diffusion occurs in the form of H_2 molecules, an increase in the defect concentration is observed, due to the creation of H-terminated dangling bonds. In addition to this, the H-terminated dangling bonds align to result in the formation of more and/or larger microvoids.

5.5 CONCLUSION

In this chapter we have reported on the defect structure of HW-deposited a-Si:H samples with different H-concentration and bonding configurations. Furthermore, the effect of isochronal annealing on the defect structure was investigated and related to changes in the H-concentration.

The dominant defect type in the samples was found to be identical, identified as the Si dangling bond complex, even though the annihilation parameters of the

samples were essentially different. The difference in the annihilation parameters was attributed to the difference in the hydrogen bonding configuration.

Doppler-broadening spectroscopy has confirmed the creation of Si dangling bonds with increasing annealing temperature in sample A, as seen by the increase in the S-parameter. However, prior to H-diffusion a change in the defect structure is observed and is caused by the creation of low concentrations of open-volume defects or microvoids. Positron lifetime spectroscopy shows evidence of vacancy clustering at 400 °C, caused by the alignment of H-terminated dangling bonds and consequently in the creation of more and/or larger open-volume defects or microvoids. Moreover, from infrared spectroscopy we can also conclude that the internal surfaces of the microvoids are not occupied with hydrogen.

As a follow-up experiment, the stability of the defect structure of sample B should enjoy immediate attention. Future experiments to the study the stability of the defect structure should include small-angle x-ray scattering (SAXS), since this technique provides information on the void shape and void fraction in a-Si:H.

REFERENCES

[5.1]   R. Krause-Rehberg and H. S. Leipner, in "Positron Annihilation in Semiconductors – Defect studies", Springer-Verlag, Berlin (1999)

[5.2]   S. Fleischer, C. D. Beling, S. Fung, W. R. Nieveen, J. E. Squire, J. Q. Zheng and M. Missous, J. Appl. Phys. **81** (1997) 190

[5.3]   D. J. Keeble, M. T. Umlor, P. Asoka-Kumar, K. G. Lynn and P. W. Cooke, Appl. Phys. Lett. **63** (1993) 87

[5.4]   P. J. Schultz and K. G. Lynn, Rev. Mod. Phys. **60** (1988) 701

[5.5]   R. Haakvoort, A. van Veen, H. Schut, M. J. van den Boogaard, A. J. M. Berntsen, S. Roorda, P. A. Stolk and A. H. Reader, AIP Conf. Proc. **303** (1994) 48

[5.6]   J. Störmer, P. Willutzki, D. T. Britton, G. Kögel, W. Triftshäuser, W. Kiunki, F. Wittman, I. Eisele, Appl. Phys. **A 61** (1995) 61

[5.7]   M. J. van den Boogaard, in "Microvoids and Hydrogen Diffusion in Hydrogenated Amorphous Silicon", Ph.D. thesis, Utrecht University, Utrecht, The Netherlands (1992)

[5.8]   M. P. Petkov, T. Marek, P. Asoka-Kumar, K. G. Lynn, R. S. Crandall and A. H. Mahan, Appl. Phys. Lett. **73** (1998) 99

[5.9]   A. Amaral, G. Lavareda, C. Nunes de Carvalho, P. Brogueira, P. M. Gordo, V. S. Subrahmanyam, C. Lopes Gil, M. Duarte Naia, A. P. de Lima, Thin Solid Films **403 – 404** (2002) 539

[5.10] D. T. Britton, A. Hempel, D. Knoesen, W. Bauer-Kugelmann and W. Triftshäuser, Nucl. Instrum. Phys. Res. **B 164 – 165** (2000) 1010

[5.11] D. T. Britton, A. Hempel, M. Härting, G. Kögel, P. Sperr, W. Triftshäuser, C. Arendse and D. Knoesen, Phys. Rev. **B 64** (2001) 075403

[5.12] M. Härting, D. T. Britton, R. Bucher, E. Minani, A. Hempel, M. Hempel, T. P. Ntsoane, C. Arendse and D. Knoesen, J. Non-Cryst. Sol. **299 – 302** (2002) 103

[5.13]   D. T. Britton, M. Härting, A. Hempel, G. Kögel, P. Sperr,
         W. Triftshäuser, M. Hempel and D. Knoesen, J. Non-Cryst. Sol. **299 –
         302** (2002) 249

[5.14]   D. T. Britton, A. Hempel and W. Triftshäuser, Phys. Rev. Lett. **87** (2001)
         217401-1

[5.15]   W. Y. Ho and C. Surya, Microelectronics Reliability **41** (2001) 913

[5.16]   D. T. Britton, M Härting, M. R. B. Teemane, S. Mills, F. M. Nortier and
         T. N. van der Walt, Appl. Surf. Sci. **116** (1997) 53

[5.17]   A. Vehanen, K. Saarinen, P. Hautojärvi and H. Huomo, Phys. Rev. **B 35**
         (1987) 4606

[5.18]   D. R. Lide, in "CRC Handbook of Chemistry and Physics – 75th Edition",
         CRC Press (1994)

[5.19]   A. Dabrowski, in "Study of Annealing of the Defect Structure in
         Hydrogenated Amorphous Silicon using Slow Positron Techniques –
         Honours Project in Physics", Department of Physics, University of Cape
         Town, Cape Town, South Africa (2000)

[5.20]   S. Mantl and W. Triftshäuser, Phys. Rev. **B 17** (1978) 1645

[5.21]   A. Hempel, A. Dabrowski, M Härting, M. Hempel, D. Knoesen,
         W. Bauer-Kugelmann, G. Kögel, W. Triftshäuser and D. T. Britton, in
         "Annealing Effects in Hydrogenated Amorphous Silicon Layers", to be
         published.

[5.22]   G. Lucovsky, Z. Zing, Z. Lu, D. R. Lee and J. L. Whitten, J. Non-Cryst.
         Solids **182** (1995) 90

[5.23]   P. A. Fedders, Phys. Rev. **B 61** (2000) 15797

[5.24]   X. Zou, Y. C. Chan, D. P. Webb, Y. W. Lam, Y. F. Hu, C. D. Beling,
         S. Fung and H. M. Weng, Phys. Rev Lett. **84** (2000) 769

SUMMARY

Hydrogenated amorphous silicon (a-Si:H) has proven to be of technological importance in applications such as solar cells, thin film transistors, liquid crystal displays and photocopiers. This is especially due to the fact that the material can be manufactured in an inexpensive deposition process, as opposed to the costly manufacturing process of crystalline silicon. More importantly, for solar cell applications, this material has a high absorption coefficient, implying that an absorber layer of thickness ~ 0.5 μm is sufficient to absorb most of the incident radiation.

However, one major detrimental disadvantage of the material is that its electronic properties degrade upon exposure to prolonged illumination and elevated temperatures. In the manufacturing of the devices the intrinsic a-Si:H layer is usually subjected to further heat treatments, e.g. post-deposition of the n- and p-doped layers. Furthermore, in subsequent use the devices may also be exposed to radiation and temperature cycling over a wide range of temperatures. Due to these complications we have investigated the thermal stability and defect structure of a-Si:H, deposited by the hot-wire chemical vapour deposition (HWCVD) process, when exposed to elevated temperatures in the range 150 – 450 °C. Particular emphasis was placed on the effect of the as-deposited hydrogen concentration and bonding configuration on changes in the network disorder, optical band gap and defect structure.

We have successfully identified the original site of H emission under thermal annealing as the $\equiv$Si–H bond, whether isolated or on the internal surfaces of voids. There is also evidence of a reduction in the $\equiv$Si–H bond strength, as illustrated in the displacement of the IR stretching band centred at ~ 2000 cm^{-1} to lower energies. The onset of H-diffusion occurs at temperatures above 200 °C.

Raman scattering confirms that no crystalline phase transitions are induced in both samples at temperatures as high as 550 °C. We have shown that the primary cause of H-diffusion is an increase in the network disorder, resulting in the creation of H-terminated Si dangling bonds and disorder-induced $\equiv$Si–H bonds. The increase in the network disorder also causes a broadening of the valence and conduction band tails, thereby pinning the valence and conduction band edges closer together and consequently resulting in a reduction in the optical band gap.

Finally, positron annihilation spectroscopy established that the dominant defect type in both samples in the as-deposited state is fundamentally identical, identified as the Si dangling bond complex. Doppler-broadening spectroscopy has confirmed the creation of H-terminated Si dangling bonds during annealing, as seen by the increase in the S-parameter. However, prior to H-diffusion a change in the defect structure is observed and is probably caused by the creation of open-volume defects or microvoids. Positron lifetime spectroscopy shows evidence of vacancy clustering at 400 °C, caused by the alignment of H-terminated dangling bonds and consequently results in the creation of open-volume defects or microvoids. Furthermore, infrared spectroscopy provides evidence that the internal surfaces of the microvoids are not occupied by molecular hydrogen.

In conclusion we present the following model for the thermal stability of HW-deposited a-Si:H:

- Under thermal annealing an increase in the network disorder causes the termination (breaking) of the $\equiv$Si–H bond, resulting in the creation of (a) mobile H, (b) H-terminated Si dangling bonds and (c) weak disorder-induced $\equiv$Si–H bonds.

- Unstable H-terminated Si dangling bonds diffuse and eventually align, thereby resulting in vacancy clustering to form low concentrations of open-volume defects or microvoids at relatively low temperatures.

- Two mobile H atoms recombine, resulting in the formation of H_2 molecules that become trapped in H-rich clusters or microvoids, which are thought to remain stable up to relatively high temperatures. Hydrogen diffusion to the surface occurs via an accumulation of H_2 molecules in high-pressure bubbles, which eventually open by explosion and consequently results in the blistering of the sample surface.

Future experiments to study the thermal stability of HW-deposited a-Si:H should include thermal desorption spectroscopy (TDS), secondary ion mass spectroscopy (SIMS), high resolution transmission electron microscopy (HR-TEM) and small-angle x-ray scattering (SAXS).